

CMS Draft Analysis Note

The content of this note is intended for CMS internal use and distribution only

2013/08/05

Head Id: 200857

Archive Id: 200887M

Archive Date: 2013/08/05

Archive Tag: trunk

Measurement of the muon charge asymmetry in inclusive $pp \rightarrow W$ production at $\sqrt{s} = 7$ TeV

The CMS Collaboration³

¹ Northeastern University

² Fermilab

³ CERN

Abstract

We report on a measurement of the muon charge asymmetry in inclusive $pp \rightarrow W+X$ production at $\sqrt{s}=7$ TeV. The data sample corresponds to an integrated luminosity of 4.7 fb^{-1} recorded by the CMS detector at the LHC. With a sample of more than 20 million $W \rightarrow \mu\nu$ events, the statistical precision is greatly improved in comparison to previous measurements. These new results provide additional constraints on the Parton Distribution Functions (PDFs) in the proton in the Björken parameter x range from 0.001 to 0.1.

This box is only visible in draft mode. Please make sure the values below make sense.

PDFAuthor: All

PDFTitle: Muon charge asymmetry in inclusive W production at 7 TeV

PDFSubject: CMS

PDFKeywords: CMS, physics, software, computing

Please also verify that the abstract does not use any user defined symbols

1 Introduction

In pp collisions, W bosons are produced primarily via the processes $u\bar{d} \rightarrow W^+$ and $d\bar{u} \rightarrow W^-$. The quark in one of the protons is predominantly a valence quark which annihilates with a sea antiquark in the other proton. Because of the presence of two valence u quarks in the proton, there is an overall excess of W^+ over W^- bosons. The inclusive ratio of total cross sections for W^+ and W^- boson production at the Large Hadron Collider (LHC) has been measured to be $1.421 \pm 0.006(\text{stat.}) \pm 0.032(\text{syst.})$ by the Compact Muon Solenoid (CMS) experiment [1] and is in agreement with predictions of the Standard Model (SM) based on various parton distribution functions (PDFs) [2, 3]. Measurements of the production asymmetry between W^+ and W^- bosons as a function of boson rapidity provide additional constraints on the u/d ratio and on the sea antiquark densities in the proton. For pp collisions at $\sqrt{s} = 7$ TeV these measurements explore the parton distributions in the proton in Björken x from 0.001 to 0.1 [4]. However, it is difficult to measure the boson rapidity production asymmetry because of the energy carried away by neutrinos in leptonic W decays. A more direct experimentally accessible quantity is the lepton charge asymmetry, defined to be

$$A(\eta) = \frac{\frac{d\sigma}{d\eta}(W^+ \rightarrow \ell^+\nu) - \frac{d\sigma}{d\eta}(W^- \rightarrow \ell^-\bar{\nu})}{\frac{d\sigma}{d\eta}(W^+ \rightarrow \ell^+\nu) + \frac{d\sigma}{d\eta}(W^- \rightarrow \ell^-\bar{\nu})},$$

where ℓ is the daughter charged lepton, η is the charged lepton pseudorapidity in the CMS lab frame ($\eta = -\ln[\tan(\frac{\theta}{2})]$ where θ is the polar angle), and $\frac{d\sigma}{d\eta}$ is the differential cross section for charged leptons from W boson decays.

High precision measurements of the W lepton asymmetry can improve our determination of PDFs. Both W lepton charge asymmetry and the W production charge asymmetry were studied in $p\bar{p}$ collisions by the CDF and D0 experiments at the Fermilab Tevatron Collider [5, 6]. The ATLAS, CMS, and LHCb experiments also reported measurements of the lepton charge asymmetry using data collected during the 2010 LHC run [7–9]. Earlier measurements of the W lepton charge asymmetry extracted from CMS data used data samples of 840 pb^{-1} [10] and 234 pb^{-1} [11] for electron and muon decay channels respectively.

The impact of CMS measurements of the lepton charge asymmetry on PDF global fits were studied by several groups [12–14], which concluded that improvements on the uncertainties of PDFs for several quark flavors can be achieved with more precise data. In this letter, we report on an update of the muon charge asymmetry using a data sample with integrated luminosity of 4.7 fb^{-1} collected by the CMS detector at the LHC in 2011. The number of $W \rightarrow \mu\nu$ events (more than 20M) in this data sample is two orders of magnitude larger than previous measurements [8]. The measurements reported here supersede previously reported preliminary results which were based on a fraction of the 2011 CMS data [10].

This letter is organized as follows. A brief description of the CMS detector is given in Section 2. The selection of $W \rightarrow \mu\nu$ candidates is described in Section 3. The corrections for residual charge-specific bias in the measurement of the muon transverse momentum and in the muon trigger, reconstruction and selection efficiency are discussed in Section 4. The extraction of the $W \rightarrow \mu\nu$ rate is described in detail in Section 5. Systematic uncertainties and the full correlation matrix are given in Section 6. The final results are presented in Section 7, followed by a summary and conclusion in Section 8.

2 CMS experiment

A detailed description of the CMS experiment is given in a previous communication [15]. The central feature of the CMS apparatus is a 6 m internal diameter and 13 m length superconducting solenoid which provides an axial field of 3.8 T. Within the field volume are the silicon pixel and strip tracker, the crystal electromagnetic calorimeter (ECAL) and the brass/scintillator hadron calorimeter (HCAL). Muons are measured in gas-ionization detectors embedded in the steel return yoke of the solenoid. The electromagnetic calorimeter consists of nearly 76 000 lead tungstate crystals which provide coverage in pseudorapidity $|\eta| < 1.479$ in the barrel region and $1.479 < |\eta| < 3.0$ in two endcap regions. A preshower detector consisting of two planes of silicon sensors interleaved with a total of $3 X_0$ of lead is located in front of the ECAL endcaps. The ECAL has an ultimate energy resolution of better than 0.5% for unconverted photons with transverse energies above 100 GeV. Muons are measured in the pseudorapidity range $|\eta| < 2.4$, with detection planes constructed of drift tubes, cathode strip chambers, and resistive plate chambers. Matching the muons to the tracks measured in the silicon tracker results in an $|\eta|$ dependent transverse momentum (p_T) resolution of about 1-5% for muon p_T in the range 25-100 GeV.

CMS uses a right-handed coordinate system, with the origin at the nominal interaction point, the x -axis pointing towards the center of the LHC, the y -axis pointing up (perpendicular to the LHC plane), and the z -axis along the anticlockwise-beam direction. The polar angle, θ , is measured from the positive z -axis and the azimuthal angle, ϕ , is measured in the x - y plane.

3 Event reconstruction

The $W \rightarrow \mu\nu$ candidates are characterized by a high- p_T muon accompanied by missing transverse momentum (\vec{E}_T), due to the escaping neutrino. Experimentally, the \vec{E}_T is determined as the negative vector sum of the transverse momenta of all particles reconstructed using a particle flow algorithm [16]. The $W \rightarrow \mu\nu$ candidates used in this analysis were collected using a set of isolated single-muon triggers with different p_T thresholds, which is the major difference from previous CMS measurements [8, 11]. The isolated muon trigger is necessary to help reduce the trigger rate while maintaining a relatively low muon p_T threshold. We use all the data-taking periods where the isolated muon trigger is not pre-scaled. Other physics processes, such as multijet production (QCD background), Drell-Yan ($Z/\gamma^* \rightarrow \ell^+\ell^-$) production, $W \rightarrow \tau\nu$ production (EWK background), and top quark pair ($t\bar{t}$) production can produce high- p_T muons and mimic $W \rightarrow \mu\nu$ signal candidates. In addition, cosmic ray muons can mimic $W \rightarrow \mu\nu$ candidates.

Monte Carlo (MC) simulation is used to help evaluate the background contributions in the data sample. Primarily, next-to-leading order (NLO) MC simulations based on the POWHEG event generator [17] interfaced with the CT10 PDF model [3] are used. The τ in the $W \rightarrow \tau\nu$ decay process is simulated by the TAUOLA MC [18]. The QCD multijet background is generated with the PYTHIA event generator [19] interfaced with the CTEQ6L PDF model [20]. All generated events are passed through the CMS detector simulation using GEANT4 [21] and then processed using a reconstruction sequence identical to that used for data. Pile-up (PU) interactions are caused by additional low-multiplicity interactions which occur in the same or slightly different beam crossing as the “hard interaction” process such as W production. For the data used in this analysis, PU is significant, corresponding to 9-10 primary interaction vertices reconstructed for each beam crossing. The PU distribution in the MC simulation is generated with a different distribution from what is observed in the data. Therefore, the MC simulation

86 is reweighted to match the distribution of the number of interactions per crossing in the data.

87 The selection criteria for muon reconstruction and identification are described in detail in pre-
 88 vious reports [22, 23]. Therefore, only a brief summary is given below. Muon candidates are
 89 reconstructed using two different algorithms: one starts with the inner silicon tracks and then
 90 requires a minimum number of matching hits in the muon chambers, and the other starts by
 91 finding tracks in the muon system and then matching them to silicon tracks. A global track fit
 92 including both the silicon track hits and muon chamber hits is performed to improve the qual-
 93 ity of the reconstructed muon candidates. The p_T of the inner silicon track is used as the muon
 94 p_T and the charge is identified from the signed curvature of the silicon track. Cosmic ray con-
 95 tamination is reduced by requiring that the distance of closest approach to the leading primary
 96 vertex is small: $|d_{xy}| < 0.2$ cm. The primary vertices in an event are ordered according to the
 97 scalar sum of the p_T^2 of associated charged tracks. The remaining cosmic ray background yield
 98 is estimated to be about 10^{-5} of the expected $W \rightarrow \mu\nu$ signal, and is therefore neglected [8]. The
 99 track-based muon isolation, Iso_{track} , is defined to be the scalar sum of transverse momentum
 100 of tracks in a cone of 0.3 (in η and ϕ) around the muon candidate. Muons are required to have
 101 $Iso_{track}/p_T < 0.1$. Only muons within $|\eta| < 2.4$ are included in the data sample.

102 In every event, muons passing the above selection criteria are ordered according to p_T , and the
 103 leading muon is selected as the $W \rightarrow \mu\nu$ candidate. In each event the $W \rightarrow \mu\nu$ candidate is
 104 required to be the particle that triggered the event. In addition, the muon is required to have
 105 $p_T > 25$ GeV, which is the lowest momentum safely above the trigger turn-on threshold. Events
 106 which have a second muon with $p_T > 15$ GeV are rejected to reduce the background from
 107 Drell-Yan dimuon events (“Drell-Yan veto”). Note that the muon p_T is corrected for bias in the
 108 measurement of the momentum (discussed below) prior to the application of the $p_T > 25$ GeV
 109 selection cut. The rejected events, predominantly $Z/\gamma^* \rightarrow \mu^+\mu^-$ events, are also used as a
 110 Drell-Yan control sample to study the modeling of the missing transverse energy (\cancel{E}_T) in data
 111 and also provides constraints on the modeling of the transverse momentum spectrum of W
 112 and Z bosons. In addition, the sample is used to set the level of the background from Drell-Yan
 113 events for which the second muon is not identified.

114 The $W \rightarrow \mu\nu$ candidates which pass the above selection criteria are divided into 11 bins in
 115 absolute value of muon pseudorapidity ($|\eta|$):

116 [0.0, 0.2], [0.2, 0.4], [0.4, 0.6], [0.6, 0.8], [0.8, 1.0], [1.0, 1.2], [1.2, 1.4], [1.4, 1.6], [1.6, 1.85], [1.85,
 117 2.1], and [2.1, 2.4].

118 The muon charge asymmetry is measured in each of the $|\eta|$ bins, along with the determination
 119 of the correlation matrix of the systematic errors between different $|\eta|$ bins.

120 4 Muon momentum correction and efficiency studies

121 After the alignment of the tracker coordinates, a residual misalignment remains which is not
 122 perfectly reproduced in the MC simulation. The misalignment leads to a charge-dependent
 123 bias in the reconstruction of muon momenta. This bias is removed by using a muon momen-
 124 tum correction. The detailed description of the method for the extraction of the momentum
 125 corrections using a sample of $Z/\gamma^* \rightarrow \mu^+\mu^-$ events is in reference [24]. Here we only provide
 126 a short summary of the method. Initially, corrections to muon momentum in bins of η and ϕ
 127 are extracted separately for positive and negative muons using the average of the $1/p_T$ spectra
 128 of muons in $Z/\gamma^* \rightarrow \mu^+\mu^-$ events. The $1/p_T$ spectra at the MC generator-level (smeared by
 129 the momentum resolution) are used as “Reference”. The means of reconstructed spectra in data

130 or MC simulation are tuned to match the “Reference”. In the second step, the corrections are
 131 tuned by comparing the dimuon invariant mass in the same bins of muon charge Q , η , and ϕ
 132 to the “Reference”. A comparison of the corrections for positive and negative muons in each
 133 bin are used to separately determine the relative contributions of bias from misalignment and
 134 bias from uncertainties of the magnetic field in the tracker system. We find that the corrections
 135 are predominantly from misalignment. The same procedure is preformed for both data and
 136 reconstructed MC events, and correction factors are determined separately for the data and
 137 reconstructed MC samples.

138 The average of the Z mass as a function of muon η (mass profile) before and after the correction
 139 is shown in Figure 1. The peak of the Z mass in the corrected distribution is compared to the
 140 nominal reference Z mass peak as a function of η for data and MC respectively. Note that
 141 the reference average Z mass is expected to be a function of η because of the effect of the
 142 transverse momentum cuts on the two muons. The mass profiles are used to further tune the
 143 muon momentum corrections. The muon momentum corrections are extracted using the same
 144 η binning as used for the asymmetry analysis in order to avoid correlations in the corrections
 145 between different η bins. As shown in Figure 1, the mass profile in data and MC simulation
 146 agrees well with the reference and the muon scale bias is removed.

147 The overall efficiency in the selection of muon candidates includes contributions from recon-
 148 struction, identification (including isolation), and trigger efficiency. The muon reconstruction
 149 efficiency includes contributions from the reconstruction efficiency in the inner tracker sys-
 150 tem (“tracking”) and in the outer muon system. The muon “offline” efficiency is the prod-
 151 uct of reconstruction and identification efficiencies. The contribution of each component to
 152 the overall efficiency (tracking, outer muon reconstruction, identification, and trigger) is mea-
 153 sured directly from the same sample of $Z/\gamma^* \rightarrow \mu^+\mu^-$ events using the Tag-and-Probe method
 154 [22]. In the Tag-and-Probe method one of the muons in the dimuon sample is used to tag the
 155 $Z/\gamma^* \rightarrow \mu^+\mu^-$ event and another muon candidate is used as a probe to study the muon ef-
 156 ficiencies as a function of Q , η , and p_T . For every event a positively charged muon can be
 157 selected as the tag and a negatively charged probe candidate is used to study the efficiencies of
 158 negatively charged muons. The same procedure is repeated by selecting a negatively charged
 159 muon as the tag to study efficiencies of positively charged muons. Each individual efficiency
 160 is determined in 22 bins of muon η as defined above and 7 bins of p_T ([15, 20, 25, 30, 35, 40,
 161 45, infinite]) for μ^+ and μ^- , respectively. The same procedure is done for both data and MC
 162 simulation and scale factors are determined to match the efficiencies in MC to the data.

163 The measured average tracking efficiency in each η bin varies from 99.6 to 99.9% with a slight
 164 inefficiency in transition regions and at the edge of the tracker system. The ratio of tracking
 165 efficiency between μ^+ and μ^- is consistent with 1.0 within statistical uncertainty. In the tran-
 166 sition regions of the muon detector, there is evidence that muon offline efficiency has a slight
 167 asymmetry between μ^+ and μ^- . The ratio of efficiencies for positive and negative muon dif-
 168 fers from 1.0 by up to $1.0 \pm 0.3\%$. The trigger efficiency ratio is also found to differ from 1.0 in
 169 some η regions. The maximum deviation is at $\eta > 2.1$ where efficiency for μ^+ is about $2.0 \pm 0.5\%$
 170 higher than for μ^- . Figure 2 shows the pseudorapidity distribution for the leading μ^+ and μ^-
 171 in the $Z/\gamma^* \rightarrow \mu^+\mu^-$ sample. Here the MC simulation is corrected for muon momentum bias,
 172 efficiency and mis-modeling of the underlying physics before normalizing to yields in data.
 173 The pseudorapidity dependence of data and MC are in very good agreement.

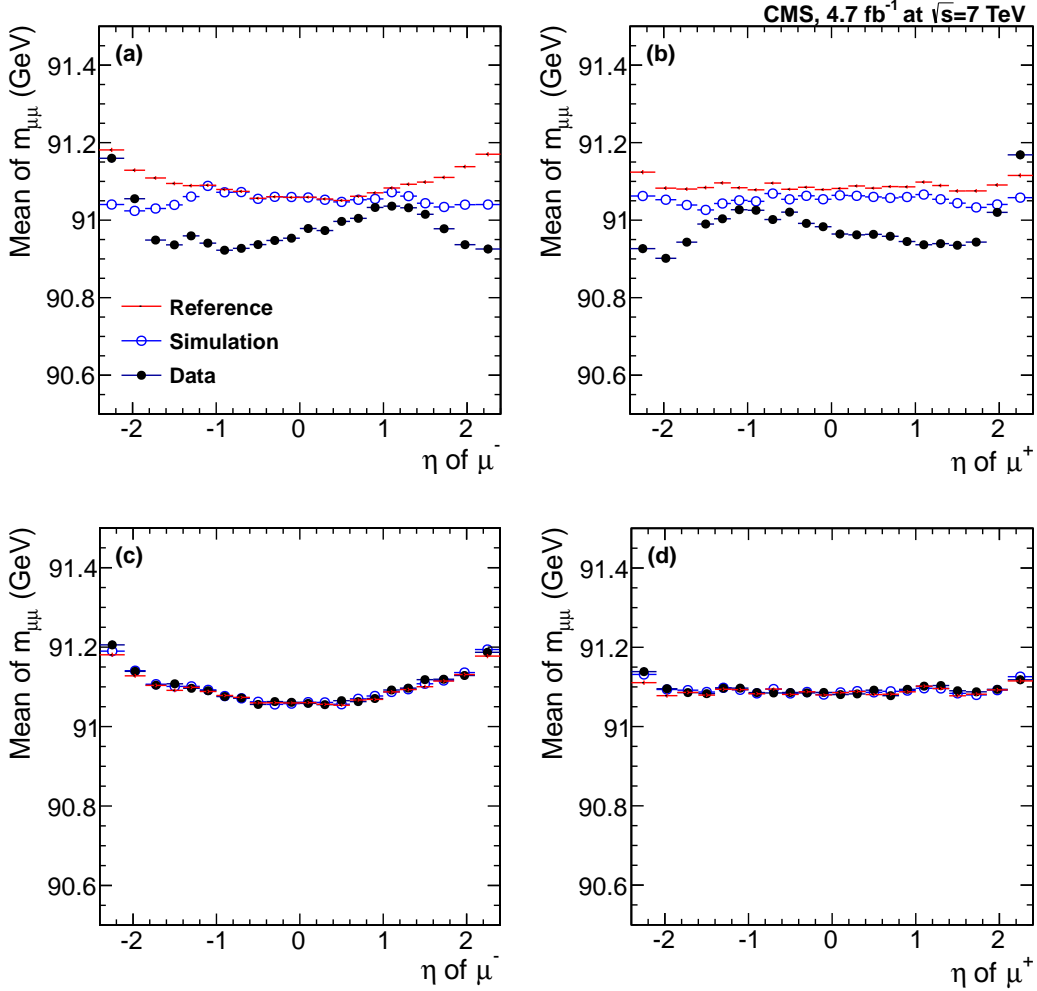


Figure 1: The Z mass profile as a function of muon η for μ^- (a, c) and μ^+ (b, d), where (a) and (b) are before the correction and (c) and (d) are after the correction.

5 Extraction of the signal for W events

174

175 After the event selection described above, there are a total of 12.9 million $W^+ \rightarrow \mu^+ \nu$ and
 176 9.1 million $W^- \rightarrow \mu^- \bar{\nu}$ candidate events. The expected backgrounds from QCD, EWK and $t\bar{t}$
 177 events in the $W \rightarrow \mu\nu$ data sample are about 8%, 8%, and 0.5%, respectively. The background
 178 composition can vary for different $|\eta|$ bins. The background from single top-quark and diboson
 179 production is less than 0.1%.

180 Binned maximum likelihood fits of the E_T distributions are simultaneously performed for W^+
 181 and W^- candidate events to extract the W^+ yield (N^{W^+}) and the W^- yield (N^{W^-}) for each $|\eta|$
 182 bin. The likelihood is constructed following the Barlow-Beeston method to take into account
 183 the finite Monte Carlo statistics [25]. The $W \rightarrow \mu\nu$ MC sample is about the same size as the $W \rightarrow$
 184 $\mu\nu$ candidates in data. To avoid the large spread of weights introduced by PU reweighting, each
 185 MC sample is matched to the data PU distribution using an “accept-reject” technique based on
 186 the data/MC PU distributions.

187 The shapes of the E_T distributions for the $W \rightarrow \mu\nu$ signal and background contributions are
 188 taken directly from MC simulations after correcting for mis-modeling of detector response and

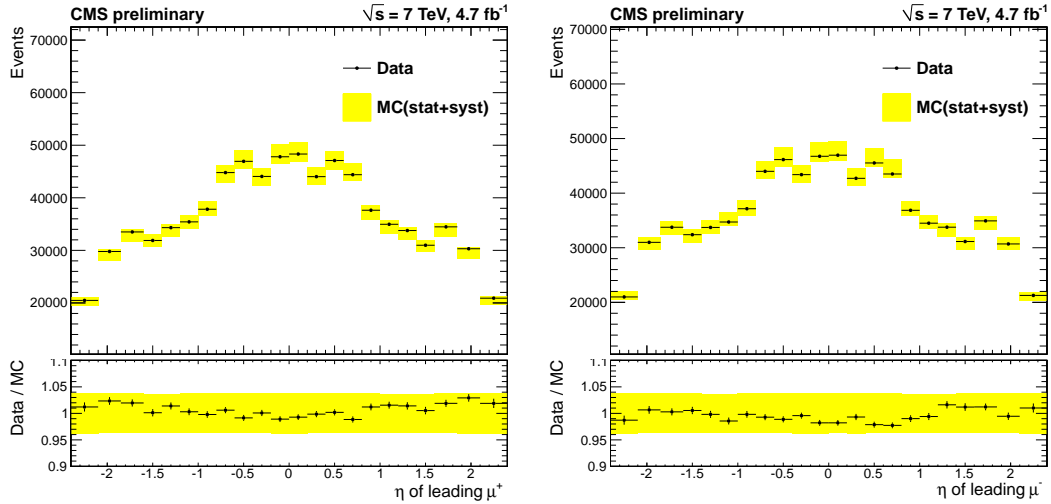


Figure 2: Pseudorapidity distribution of the leading μ^+ (left) and the μ^- (right) in $Z/\gamma^* \rightarrow \mu^+\mu^-$ sample. The dimuon invariant mass is within $60 < m_{\mu\mu} < 120$ GeV. The MC simulation is normalized to data yields. The yellow band is the total uncertainty in predicting the $Z/\gamma^* \rightarrow \mu^+\mu^-$ event yields using MC simulation, as described in Section 6.

189 underlying physics. The normalizations of N^{W^+} , N^{W^-} , and QCD backgrounds are allowed to
 190 float. The ratio of the QCD backgrounds for W^+ and W^- candidate events is fixed using a QCD-
 191 enriched data control sample, which was collected using a non-isolated muon trigger. The
 192 Drell-Yan production cross section is rescaled using the yields in the Drell-Yan control sample,
 193 and the expected Drell-Yan background is normalized using this rescaled normalization factor.
 194 The $W \rightarrow \tau\nu$ background is normalized to the $W \rightarrow \mu\nu$ yield in data and the ratio of $W \rightarrow \tau\nu$
 195 to $W \rightarrow \mu\nu$ is determined from MC simulation. The $t\bar{t}$ background is normalized to the QCD-
 196 NLO cross sections obtained from MCFM [26]. Note that the efficiency in the MC is scaled to
 197 match the efficiency in the data before the extraction of the background normalization factors.
 198 The number of N^W signal events is extracted from the two fitted normalization factors and MC
 199 W yields.

The observed raw charge asymmetry (\mathcal{A}^{raw}) is related to the N^{W^+} and N^{W^-} by the following equation,

$$\mathcal{A}^{raw} = \frac{N^{W^+} - N^{W^-}}{N^{W^+} + N^{W^-}}. \quad (1)$$

200 Fixing the ratio of QCD background between W^+ and W^- candidate events introduces a cor-
 201 relation between the two normalization factors. This is taken into account in the extraction of
 202 N^{W^+} , N^{W^-} and raw charge asymmetry (\mathcal{A}^{raw}).

203 The simulation of the \vec{E}_T distribution in the CMS $Z/\gamma^* \rightarrow \mu^+\mu^-$ MC samples is not in per-
 204 fect agreement with what is observed in data. A Φ -modulation of the \vec{E}_T is observed in both
 205 data and MC simulation, where the phase and amplitude of the modulation is different be-
 206 tween data and simulation. Different sources, such as PU, mis-alignment within sub-detectors
 207 or between different sub-systems, and mis-modeling of detector response in simulation, can
 208 contribute to differences in the \vec{E}_T distributions for data and MC. In this analysis, the PU dis-
 209 tribution in the MC simulation is reweighted to match the number of events per crossing seen
 210 in the data. In addition, the \vec{E}_T is corrected for the muon momentum scale bias as described in
 211 Section 4. This is done by adding the muon p_T scale correction vectorially to the \vec{E}_T in data and
 212 MC simulation, respectively. However, a disagreement remains at a significant level which can

213 potentially result in large systematic uncertainty in the measured charge asymmetry. Therefore,
 214 the $Z/\gamma^* \rightarrow \mu^+\mu^-$ control sample is used to empirically parametrize the mis-modeling to im-
 215 prove data-MC agreement. We use the “hadronic-recoil” technique (which has been previously
 216 used in both Tevatron experiments and in CMS [27–29]), as described below.

217 5.1 Definition of the “hadronic recoil”

The “hadronic recoil”, \vec{u} , is defined as a vector sum of transverse momenta of all particle can-
 didates excluding the candidate muon(s). In $W \rightarrow \mu\nu$ events, it is related to the \vec{E}_T as follows,

$$\vec{u} = -\vec{E}_T - \vec{p}_T, \quad (2)$$

where \vec{p}_T is the muon transverse momentum. In $Z/\gamma^* \rightarrow \mu^+\mu^-$ events, it is defined to be

$$\vec{u} = -\vec{E}_T - \vec{q}_T \quad (3)$$

218 where \vec{q}_T is the transverse momentum of the di-muon system.

219 In the $Z/\gamma^* \rightarrow \mu^+\mu^-$ event sample, the parallel and perpendicular component of \vec{u} relative to
 220 boson \vec{q}_T are defined as $u_{||}$ and u_{\perp} respectively. The mean of u_{\perp} , \tilde{u}_{\perp} , is about 0. The mean of
 221 $u_{||}$, average recoil $\tilde{u}_{||}$, is close to the mean of the boson q_T , which is the detector response to the
 222 hadronic activity recoiling against the boson transverse momentum. The data-MC difference
 223 of the hadronic recoil distributions seen in the $Z/\gamma^* \rightarrow \mu^+\mu^-$ sample is used to improve the
 224 the modeling of the \vec{E}_T in the MC for W events and other physics processes. The procedure of
 225 extracting empirical corrections from the $Z/\gamma^* \rightarrow \mu^+\mu^-$ sample and applying them to other
 226 physics processes is described below.

227 5.2 Correction procedure

The first step in the procedure is to correct the \vec{E}_T for both the muon scale bias described in
 Section 4, and the Φ -modulation described above. The Φ -modulation of \vec{E}_T is largely due to
 the fact that collisions, including hard-interactions that produce W events as well as PU events
 do not occur exactly at the origin of the CMS lab frame. This modulation can be characterized
 by a cosine function, $C \cdot \cos(\Phi - \Phi_0)$. The dependence of the amplitude C and phase term
 Φ_0 on the number of offline primary vertices (n) is extracted from the $Z/\gamma^* \rightarrow \mu^+\mu^-$ event
 sample. This is done by fitting the Φ -dependent $(u_{||} - \tilde{u}_{||})(q_T)$ profile. Here the $\tilde{u}_{||}(q_T)$ can be
 parametrized by

$$- \tilde{u}_{||}(q_T) = (c_0 + c_1 q_T) \left(1 + \text{erf}(\alpha q_T^\beta) \right), \quad (4)$$

228 where c_0 , c_1 , α , and β are floating parameters and $\text{erf}(x)$ is the error function. The amplitude
 229 C is found to have linear dependence on the number of primary vertices n , while the Φ_0 is
 230 almost independent of PU. The measured C and Φ_0 distributions are different between the
 231 $Z/\gamma^* \rightarrow \mu^+\mu^-$ data sample and the corresponding MC simulation. The Φ -modulation of \vec{E}_T
 232 can be removed by adding a 2-D vector $(C \cos(\Phi_0), C \sin(\Phi_0))$ to the \vec{E}_T distribution, with C
 233 and Φ_0 extracted from $Z/\gamma^* \rightarrow \mu^+\mu^-$ events.

The second step is to determine the hadronic recoil in $Z/\gamma^* \rightarrow \mu^+\mu^-$ events. The $\tilde{u}_{||}(q_T)$ is
 measured as a function of boson q_T in 4 bins of leading jet $|\eta_j|$: [0.0, 1.2], [1.2, 2.4], [2.4, 3.0], and
 [3.0, 5.0]. The jets are formed by clustering particle flow candidates using anti- k_T jet clustering
 algorithm with cone size 0.5 [30]. The identified muon candidates are removed prior to the jet
 reconstruction. In each $|\eta_j|$ bin, the q_T -dependence of $\tilde{u}_{||}(q_T)$ is parametrized by Eq. 4. The
 resolutions of $u_{||}$ and u_{\perp} in each boson q_T are determined by fitting a Gaussian function to the

$u_{\parallel} - \tilde{u}_{\parallel}$ and u_{\perp} distributions, respectively. This is done as a function of the number of primary vertices n . The fitted Gaussian widths as a function of q_T for different number of primary vertices are parametrized by the following function,

$$\sigma(q_T; n) = \sqrt{N_n^2 + S_n^2 q_T}, \quad (5)$$

234 where N_n , S_n are parameters extracted from the fit. The average recoil and resolutions are
 235 extracted for both $Z/\gamma^* \rightarrow \mu^+\mu^-$ data and MC simulation, respectively.

236 The last step is to apply the average recoil and resolution extracted from $Z/\gamma^* \rightarrow \mu^+\mu^-$ events
 237 to improve the agreement of the \cancel{E}_T distribution between data and MC simulation. As a self-
 238 closure test, in the $Z/\gamma^* \rightarrow \mu^+\mu^-$ events the u_{\parallel} in MC simulation is shifted by the data/MC
 239 difference of the average recoil and additional smearing in u_{\parallel} and u_{\perp} is introduced to match the
 240 recoil resolutions in data. This is done on an event-by-event basis. The \cancel{E}_T is then recalculated
 241 using the corrected \vec{u} with Eq. 3. Figure 3 shows the \cancel{E}_T and the Φ distributions of $\vec{\cancel{E}}_T$ ($\Phi(\cancel{E}_T)$)
 242 after applying the hadronic recoil correction. The data and MC simulation are in excellent
 243 agreement as expected. This demonstrates that this empirical correction to \cancel{E}_T in the MC works
 very well for $Z/\gamma^* \rightarrow \mu^+\mu^-$ events. To apply the hadronic recoil correction determined in

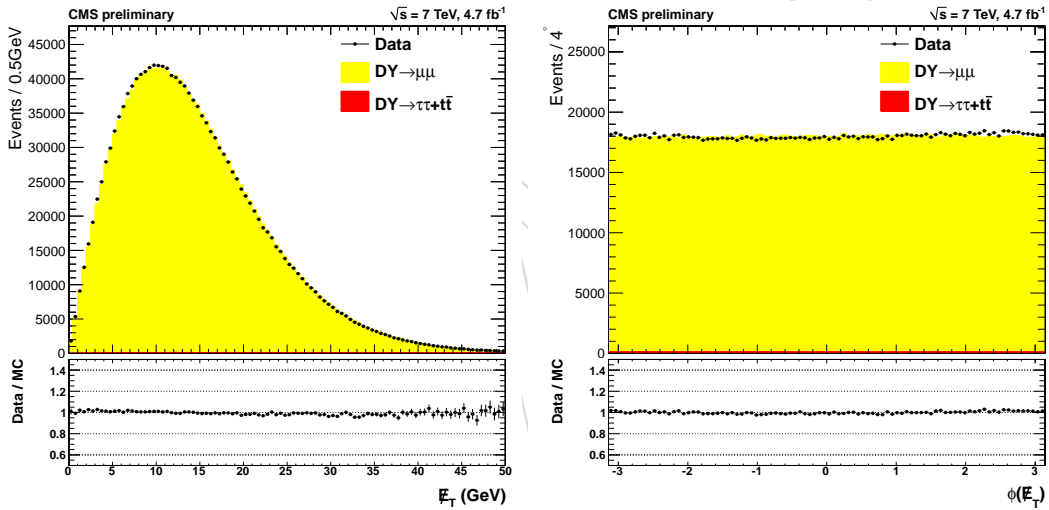


Figure 3: Data-MC comparison for \cancel{E}_T (left) and Φ of the missing transverse momentum ($\Phi(\cancel{E}_T)$) (right) in the Drell-Yan control sample. Here, the hadronic recoil derived from the data was used to correct the MC simulation. The $Z/\gamma^* \rightarrow \tau^+\tau^- + t\bar{t}$ contribution in data is normalized to the data luminosity using a MC simulation, and the normalization of $Z/\gamma^* \rightarrow \mu^+\mu^-$ MC simulation is allowed to float so that the total number of simulated MC events is normalized to the data.

244 $Z/\gamma^* \rightarrow \mu^+\mu^-$ events to other MC simulation, such as $W \rightarrow \mu\nu$ events, involves defining a
 245 variable equivalent to the boson \vec{q}_T in $Z/\gamma^* \rightarrow \mu^+\mu^-$ events. With the properly defined \vec{q}_T ,
 246 the hadronic recoil as defined in Eq. 2 is decomposed into u_{\parallel} and u_{\perp} components relative to
 247 the \vec{q}_T , and the hadronic recoil correction is applied in the same way as in the $Z/\gamma^* \rightarrow \mu^+\mu^-$
 248 MC simulation to correct for hadronic recoil and re-calculate the \cancel{E}_T . For the $W \rightarrow \mu\nu$ MC
 249 simulation, the vector sum of transverse momentum of reconstructed muon and the generated
 250 neutrino is defined to be the \vec{q}_T , while for $W \rightarrow \tau\nu$ events the generated W boson \vec{q}_T is used. For
 251 Drell-Yan background events, which pass the Drell-Yan veto, the second muon could fail some
 252 of the muon quality selection criteria, or fall outside the detector acceptance. The vector sum
 253

254 of transverse momentum of the generator-level second muon and the reconstructed muon is
 255 defined to be the \vec{q}_T^+ . For the QCD background, the \vec{q}_T^+ is defined to be the transverse momentum
 256 of the leading muon. Figure 4 shows the \cancel{E}_T distribution for the QCD control sample, where
 257 events were collected with a pre-scaled non-isolated muon trigger. Here we select events which
 258 fail the isolated muon trigger requirements. We also impose an anti-isolation selection cut
 259 $Iso_{trk}/p_T > 0.1$. For this QCD background dominated control sample, data and MC are in very
 good agreement after the application of the recoil corrections.

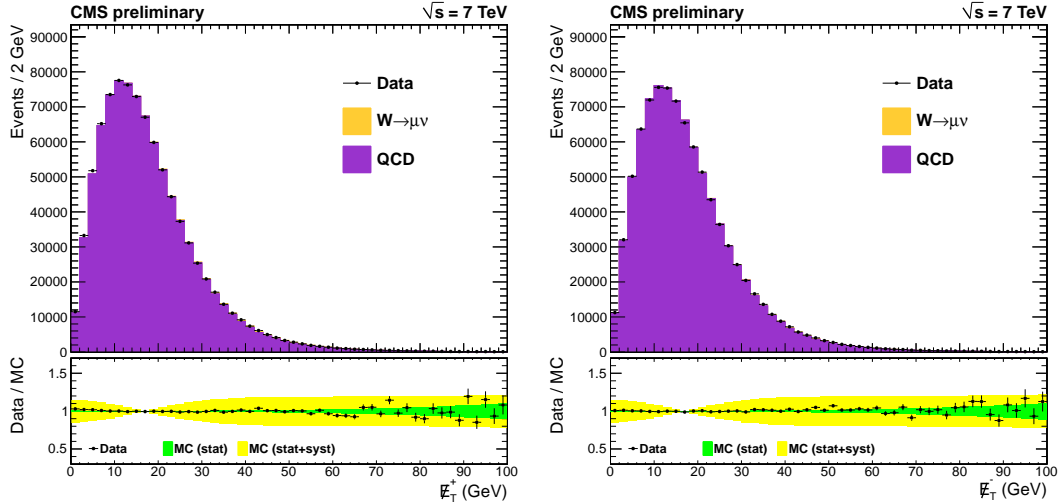


Figure 4: Data-MC comparison of the \cancel{E}_T distribution for μ^+ (\cancel{E}_T^+) (left), and μ^- (\cancel{E}_T^-) (right) in a QCD background dominated sample. The hadronic recoil derived from data was used to correct the MC simulation. The $W \rightarrow \mu\nu$ contribution in data is normalized to data luminosity using MC simulation and the normalization of the QCD simulation is allowed to float so that total number of MC simulated events is normalized to the data. The green band in each ratio plot shows the statistical uncertainty of the QCD MC \cancel{E}_T shape and the yellow band shows the total uncertainty, including all systematic uncertainties as discussed in Section 6.

260

261 5.3 Extraction of the asymmetry from fits to the \cancel{E}_T distributions

262 The $W \rightarrow \mu\nu$ signal is extracted from fits to the \cancel{E}_T distributions of $W \rightarrow \mu\nu$ candidates as
 263 shown in Figure 5. Fits are shown for three $|\eta|$ bins: $0.0 \leq |\eta| < 0.2$, $1.0 \leq |\eta| < 1.2$,
 264 and $2.1 \leq |\eta| < 2.4$, respectively. The \cancel{E}_T distributions for the $W \rightarrow \mu\nu$ signal and back-
 265 grounds are obtained from simulations which are corrected for the hadronic recoil as measured
 266 in $Z/\gamma^* \rightarrow \mu^+\mu^-$ events. The ratios between the data points and the final fits are shown on the
 267 bottom of each panel. Table 1 summarizes the fitted N^{W^+} , N^{W^-} , correlation between N^{W^+} and
 268 N^{W^-} ($\rho_{(N^{W^+}, N^{W^-})}$), raw charge asymmetry (\mathcal{A}^{raw}), and χ^2 value of the fit for each $|\eta|$ bin. The
 269 χ^2 values show that the fit model describes the data well. The raw charge asymmetry \mathcal{A}^{raw}
 270 is calculated using Eq. 1. Here, the correlations between signal yields N^{W^+} and N^{W^-} are taken
 271 into account to estimate the error on the \mathcal{A}^{raw} . This correlation is about 10–15% and varies
 272 from bin to bin. The raw charge asymmetry is further corrected for possible detector bias as
 273 discussed in the sections below.

274 We also repeat the analysis with a higher muon p_T threshold of 35 GeV. For this higher thresh-
 275 old, the lepton charge asymmetry is forced to be closer to the W-boson charge asymmetry due
 276 to kinematic constraints. Therefore, theoretical predictions for the asymmetry are different. For

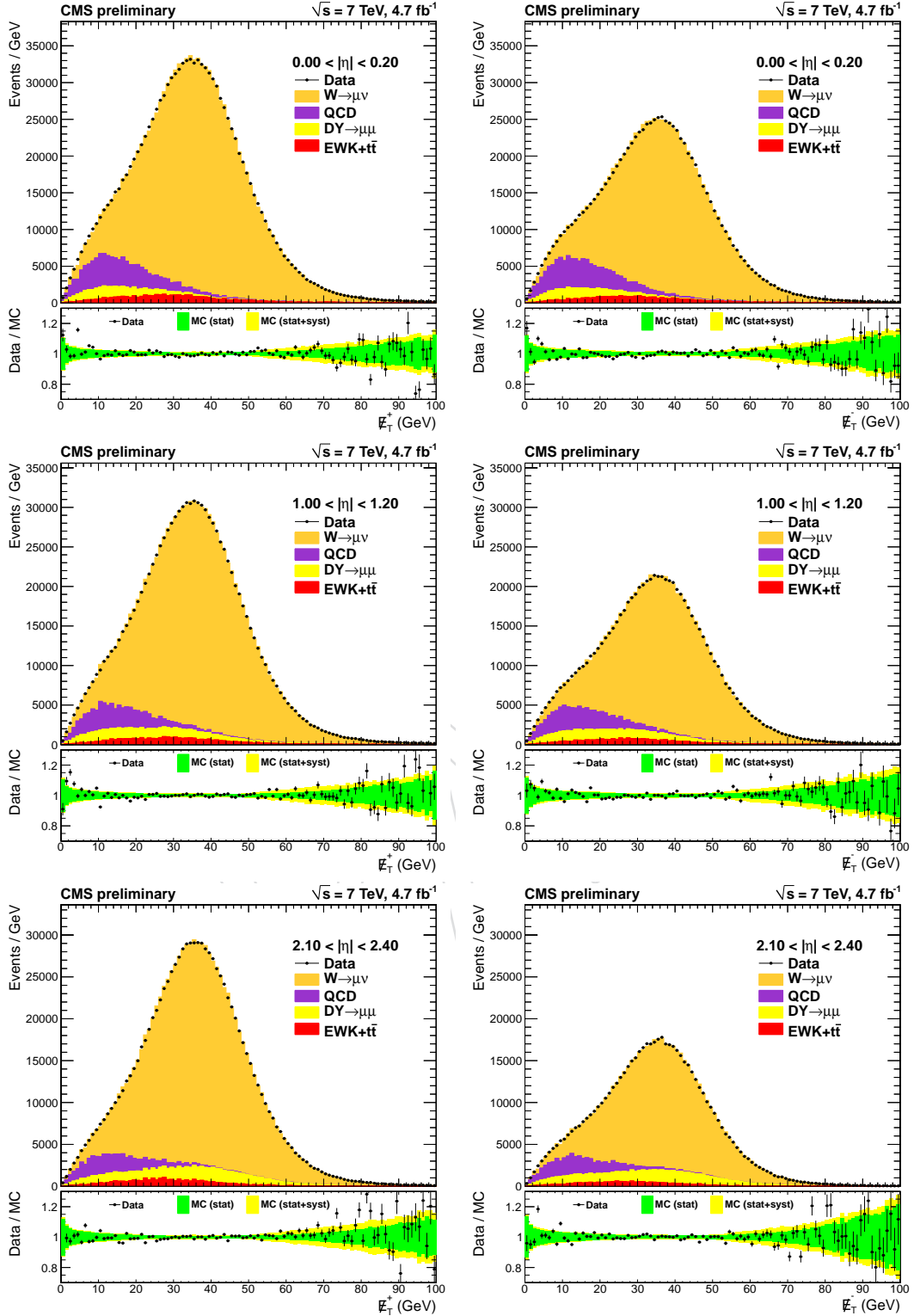


Figure 5: Muon $p_T > 25$ GeV data sample. Examples of the extraction of the $W \rightarrow \mu\nu$ signal from fits to E_T distributions of $W \rightarrow \mu\nu$ candidates in data: $0.0 \leq |\eta| < 0.2$ (top), $1.0 \leq |\eta| < 1.2$ (middle), and $2.1 \leq |\eta| < 2.4$ (bottom). The fits to $W^+ \rightarrow \mu^+\nu$ and $W^- \rightarrow \mu^-\bar{\nu}$ candidates are on the left and right figures, respectively. The ratios between the data points and the final fits are shown on the bottom of each panel. The green band in each ratio plot shows the statistical uncertainty in the shape of the MC E_T distribution, and the yellow band shows the total uncertainty, including all systematic uncertainties as discussed in Section 6.

Table 1: Summary of the fitted N^{W^+} , N^{W^-} , correlation between N^{W^+} and N^{W^-} ($\rho_{(N^{W^+}, N^{W^-})}$), the fit χ^2 and raw charge asymmetry (\mathcal{A}^{raw}) for each $|\eta|$ bin. The $\rho_{(N^{W^+}, N^{W^-})}$ and \mathcal{A}^{raw} are in units of percent.

$ \eta $ bin	$N^{W^+} (\times 10^3)$	$N^{W^-} (\times 10^3)$	$\rho_{(N^{W^+}, N^{W^-})}$	χ^2 (NDF=197)	\mathcal{A}^{raw} (%)
$p_T > 25$ GeV					
0.00-0.20	1033.0 ± 1.4	764.9 ± 1.2	14.5	255	14.912 ± 0.096
0.20-0.40	970.2 ± 1.3	713.9 ± 1.2	14.9	190	15.216 ± 0.098
0.40-0.60	1060.3 ± 1.4	771.5 ± 1.2	14.7	220	15.766 ± 0.094
0.60-0.80	1055.1 ± 1.4	752.4 ± 1.2	14.6	213	16.745 ± 0.093
0.80-1.00	935.8 ± 1.3	652.1 ± 1.1	14.5	245	17.866 ± 0.098
1.00-1.20	931.0 ± 1.3	625.4 ± 1.1	13.9	231	19.636 ± 0.099
1.20-1.40	949.0 ± 1.3	621.6 ± 1.1	14.2	209	20.848 ± 0.099
1.40-1.60	957.1 ± 1.3	607.3 ± 1.1	13.7	202	22.365 ± 0.099
1.60-1.85	1131.8 ± 1.4	687.6 ± 1.2	14.7	225	24.417 ± 0.093
1.85-2.10	1113.4 ± 1.4	656.8 ± 1.1	12.9	237	25.797 ± 0.094
2.10-2.40	843.6 ± 1.2	481.3 ± 1.0	11.8	244	27.341 ± 0.106
$p_T > 35$ GeV					
0.00-0.20	574.3 ± 1.0	459.7 ± 0.9	18.9	203	11.083 ± 0.116
0.20-0.40	538.9 ± 0.9	428.9 ± 0.9	17.4	202	11.371 ± 0.119
0.40-0.60	588.3 ± 1.0	462.8 ± 0.9	18.5	187	11.935 ± 0.114
0.60-0.80	582.9 ± 1.0	453.7 ± 0.9	18.7	205	12.472 ± 0.114
0.80-1.00	513.7 ± 0.9	392.3 ± 0.8	18.7	218	13.406 ± 0.124
1.00-1.20	509.1 ± 0.9	379.2 ± 0.8	15.7	226	14.620 ± 0.121
1.20-1.40	520.2 ± 0.9	376.9 ± 0.8	16.2	191	15.970 ± 0.123
1.40-1.60	522.7 ± 0.9	370.2 ± 0.8	14.7	195	17.074 ± 0.123
1.60-1.85	614.6 ± 1.0	418.8 ± 0.9	17.5	239	18.945 ± 0.118
1.85-2.10	604.7 ± 1.0	395.8 ± 0.9	15.0	192	20.885 ± 0.123
2.10-2.40	464.3 ± 0.9	288.5 ± 0.8	14.7	234	23.357 ± 0.141

277 a higher muon p_T threshold, the background compositions are significantly different. The ex-
 278 pected QCD background is reduced to about 1% in the $W \rightarrow \mu\nu$ candidate sample. The $p_T > 35$
 279 GeV sample provides a cross check of the analysis method. Note that the $W \rightarrow \mu\nu$ candidates
 280 with $p_T > 35$ GeV are included in the measurement for $p_T > 25$ GeV. The results with muon p_T
 281 threshold of 35 GeV are also summarized in Table 1.

282 6 Systematic uncertainties

283 In order to compare the experimental results to theoretical predictions, we investigate possible
 284 additional corrections to the raw charge asymmetry (\mathcal{A}^{raw}) from detector bias that results in a
 285 difference from the true charge asymmetry (\mathcal{A}^{true}). For the MC simulation \mathcal{A}^{true} is defined as
 286 the asymmetry at the generator level.

287 One possible bias can originate from muon charge mis-identification (w), which can dilute
 288 charge asymmetry by a factor of $(1 - 2w) \cdot \mathcal{A}^{true}$. The muon charge misidentification rate

was studied in detail and was shown to have negligible effect on the charge asymmetry [8]. The muon momentum resolution can also smear the \mathcal{A}^{true} . The resolution on the measurement of muon momentum is estimated to be in the 1.5-5.0% range depending on muon η [23]. The uncertainty on the muon momentum correction can also contribute an additional systematic uncertainty in the signal estimation and is discussed below. The impact of QED final-state-radiation (FSR) on the muon charge asymmetry has also been previously studied using POWHEG MC samples and a reduction of the asymmetry at the level of 0.07% or less is found [8] for $W \rightarrow \mu\nu$ decays. Recent theoretical calculations could combine FSR and NLO electro-weak and next-to-next-to-leading order (NNLO) QCD corrections [31]. Therefore no FSR correction is applied to the measurement.

A difference in the efficiency for μ^+ and μ^- can bias the measured charge asymmetry. We can correct for a difference in the efficiency for μ^+ and μ^- events using the following expression,

$$\mathcal{A}^{true} = \mathcal{A}^{raw} - \frac{1 - (\mathcal{A}^{raw})^2}{2} \left(r^{W^+/W^-} - 1 \right), \quad (6)$$

where r^{W^+/W^-} is the ratio of the selection efficiency between W^+ and W^- events. The systematic uncertainty from a possible efficiency difference between the μ^+ and μ^- on the extraction of \mathcal{A}^{raw} is discussed below.

For studies of some of the systematic uncertainties, we generate a large number of pseudo-experiments and repeat the entire analysis for each pseudo-experiment. This method is used to determine the uncertainties in the asymmetry from the muon scale correction, event selection and from the \cancel{E}_T correction. The resulting extracted raw charge asymmetries are used to determine corrections to the asymmetry and assign systematic uncertainties.

6.1 Efficiency ratio

As discussed previously, the muon offline and trigger efficiencies are measured in 7 p_T bins and 22 η bins for μ^+ and μ^- , respectively. The offline efficiency ratio between μ^+ and μ^- is very close to 1 in most of the detector regions. However, there is evidence that the ratio deviates from 1 in the transition regions between detectors.

We correct for the efficiency bias in the detector using the muon efficiencies determined from $Z/\gamma^* \rightarrow \mu^+\mu^-$ data and MC simulation. For each $|\eta|$ bin an average W selection efficiency $\epsilon(W^\pm)$ is obtained from the following expression,

$$\epsilon(W^\pm) = \frac{\sum(k \cdot \epsilon^{\mu^\pm, data}(p_T, \eta) / \epsilon^{\mu^\pm, MC}(p_T, \eta))}{\sum(k / \epsilon^{\mu^\pm, MC}(p_T, \eta))}, \quad (7)$$

where $\epsilon^{\mu^\pm, data}(p_T, \eta)$, $\epsilon^{\mu^\pm, MC}(p_T, \eta)$ are total muon efficiencies and k are additional event-by-event weights introduced by W boson q_T reweighting described below. The PU difference between data and MC has been corrected for using the ‘‘accept-reject’’ technique based on data/MC PU distributions. The ratio (r^{W^+/W^-}) between $\epsilon(W^+)$ and $\epsilon(W^-)$ is used to correct for the raw charge asymmetry following Eq. 6. In addition, the muon efficiency affects the background normalization since the $t\bar{t}$ background is normalized to the data luminosity. All MC samples are corrected for any data/MC efficiency difference.

To estimate the systematic uncertainty from the muon efficiencies, the muon efficiency values in data and MC simulation are modified according to their errors independently in each p_T - η bin. Many pseudo-efficiency tables are generated. In each pseudo-experiment the efficiency values are used to correct the MC simulation, fix the $t\bar{t}$ background normalization and measure

323 \mathcal{A}^{raw} . \mathcal{A}^{raw} is further corrected for W selection efficiency ratio r^{W^+/W^-} as described above. The
 324 RMS of the resulting asymmetry distribution is treated as the systematic error originating from
 325 the uncertainty in the determination of the ratio of the muon efficiencies. The mean of the \mathcal{A}^{raw}
 326 distribution is taken as the corrected charge asymmetry. In this study, the variations for differ-
 327 ent $|\eta|$ bins are completely independent from each other. Therefore, the systematic uncertainty
 328 from uncertainties in the efficiency ratio are assumed to have zero correlation between different
 329 $|\eta|$ bins. This is one of the dominant systematic uncertainties.

330 As a cross check, Figure 6 shows a comparison of the measured muon charge asymmetry be-
 331 tween positive pseudorapidity ($\eta > 0$) and negative pseudorapidity ($\eta < 0$) regions. This is
 332 done by performing identical measurement in 22 muon η bins. We find that the charge asym-
 metries for $\eta > 0$ and $\eta < 0$ are in very good agreement with each other.

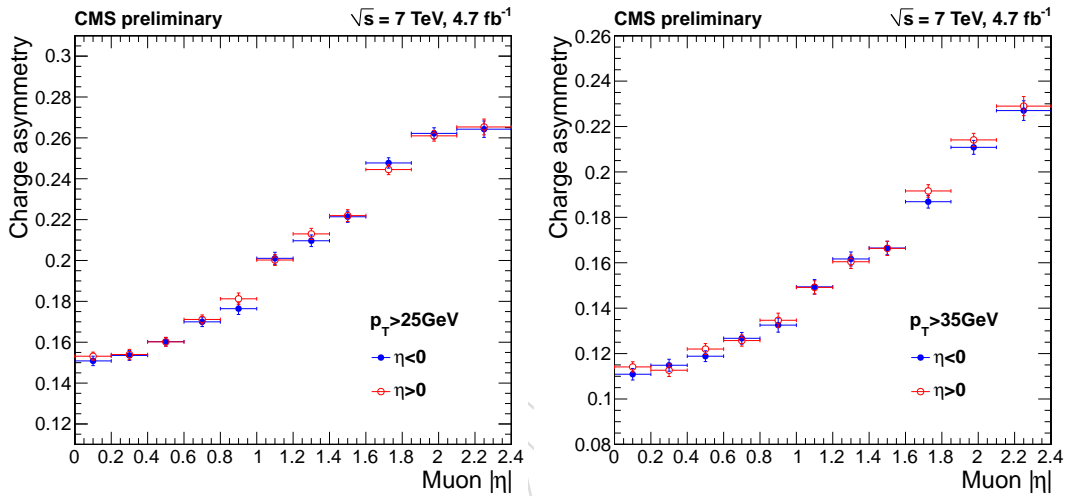


Figure 6: Comparison of the final muon charge asymmetry (\mathcal{A}) extracted for the positive pseudorapidity ($\eta > 0$) and negative pseudorapidity ($\eta < 0$) regions for the muon $p_T > 25$ GeV (left) and muon $p_T > 35$ GeV (right) samples. The uncertainties include only the statistical uncertainty from the signal extraction and uncertainty in the determination of the efficiencies for positive and negative muons.

333

334 6.2 Extraction of the signal of the W lepton charge asymmetry

335 The remaining systematic uncertainties in the extraction of the W lepton charge asymmetry
 336 originate from QCD background, correction for muon scale, Drell-Yan background normal-
 337 ization, \cancel{E}_T modeling, PU reweighting, PDF uncertainty, integrated luminosity, $t\bar{t}$ background,
 338 $W \rightarrow \tau\nu$ background, and W boson q_T modeling. Among these systematic sources, the QCD
 339 background and correction for muon scale are the largest. In the following subsections each
 340 source of systematic uncertainty is discussed in detail and correlations between different $|\eta|$ -
 341 bins are investigated to construct the correlation matrix among the total systematic uncertain-
 342 ties.

343 6.2.1 QCD background

344 The total QCD background normalization is allowed to float in the fit for the signal and the
 345 ratio of the QCD backgrounds in W^+ and W^- is fixed to the ratio observed in the QCD control
 346 region. There are two sources of the systematic error in the QCD background. The first is

347 related to fixing the ratio of the backgrounds in the W^+ and W^- samples (“QCD +/-”), and the
 348 second is related to the modeling of the shape of the QCD \cancel{E}_T distribution (“QCD shape”).

349 To evaluate the systematic uncertainty from “QCD +/-”, the ratio is varied by $\pm 5\%$ and $\pm 15\%$
 350 for muon p_T thresholds of 25 GeV and 35 GeV, respectively. The resulting shifts in the raw
 351 charge asymmetry are taken as one source of systematic error. For the last $|\eta|$ bin, this variation
 352 is 10% and 20%, respectively. These variations of the ratio span the maximum range indicated
 353 by the QCD MC simulation. As an additional cross check we fix the QCD shape to be the same
 354 for μ^+ and μ^- and allow the two QCD normalizations to float in the extraction of the signal.
 355 We find that the fitted values for the ratio of the QCD backgrounds for W^+ and W^- are within
 356 the variations quoted above.

357 The second source of systematic error is a possible difference in the shape for the QCD back-
 358 ground for W^+ and W^- . The QCD \cancel{E}_T shape has been taken from MC simulation and additional
 359 recoil correction has been applied. Two types of variations in the shape of the QCD \cancel{E}_T distri-
 360 bution are considered. First, the shape of the QCD \cancel{E}_T distribution without the hadronic recoil
 361 correction is used in the extraction of the signal. This is done in a correlated way for the W^+
 362 and W^- samples. Secondly, the shapes of the QCD \cancel{E}_T distribution are varied separately for the
 363 W^+ and W^- samples (within the statistical uncertainty) and the resulting shapes are used in
 364 the signal extraction. The two contributions to the systematic error from the “QCD shape” are
 365 added in quadrature.

366 The above procedure has been performed independently from bin to bin. Therefore the bin-
 367 to-bin correlation of these uncertainties in the asymmetries is assumed to be zero. In total,
 368 systematic uncertainty due to QCD background is comparable to the one from determining the
 369 muon efficiencies.

370 6.2.2 Muon momentum correction

371 The muon momentum correction affects both yields and the shape of the \cancel{E}_T distribution. To
 372 estimate the systematic error from this source the muon $1/p_T$ correction parameters in each
 373 $\eta - \phi$ bin and the muon scale global correction parameters are smeared within their errors
 374 400 times. Each time the event yields can be slightly different in both data and MC, and the
 375 extraction of the asymmetry is done for each of the 100 cases. The RMS of the measured \mathcal{A}^{raw}
 376 distribution in each muon $|\eta|$ bin is taken as systematic uncertainty and bin -to-bin correlations
 377 are zero.

378 The systematic uncertainty from the muon momentum correction is typically less than 40% of
 379 the error from the muon efficiency for the $p_T > 25$ GeV sample. However, the two errors are
 380 comparable for the $p_T > 35$ GeV sample for two reasons. First, the charge dependent bias from
 381 the alignment increases with p_T . Secondly since the Jacobian peak of the $W \rightarrow \mu\nu$ events is
 382 close to 35 GeV the local slope of the muon p_T spectrum is larger in this region.

383 6.2.3 PDF uncertainty

384 The PDF4LHC recommendation [32] is followed in the evaluation of the systematic uncertain-
 385 ties originating from uncertainties in PDF. The MSTW2008 [2], CT10 [3], and NNPDF2.3 [33]
 386 NLO PDF sets are used. All simulated events are reweighted to a given PDF set and the overall
 387 normalization is allowed to float. In this way both the uncertainties on the total cross-sections
 388 as well as in the shape of the \cancel{E}_T distribution are considered. To estimate the systematic un-
 389 certainty for CT10 and MSTW2008 sets, asymmetric master equations are used [2, 3]. For
 390 CT10 the 90% C.L. uncertainty is rescaled to 68% C.L. by dividing by a factor of 1.64485. For

391 NNPDF2.3 PDF set the RMS of the \mathcal{A}^{raw} distributions is taken. The half-width of the maximum
 392 deviation from combining all three PDF uncertainty bands is taken as the PDF uncertainty.

393 The CT10 error set is used to estimate the bin-to-bin correlations. For each pair of the PDF
 394 subsets due to the variation of the 26 PDF parameters, we reweight MC simulation and perform
 395 the signal extraction. From the resulting set of asymmetries, we estimate the uncertainties as
 396 follows:

- 397 • the maximum deviation from default asymmetry value is taken as uncertainty: $\Delta\mathcal{A}^i =$
 398 $\max(|\mathcal{A}_p^i - \mathcal{A}_0^i|, |\mathcal{A}_m^i - \mathcal{A}_0^i|)$ with i the parameter index.
- 399 • bin-to-bin correlation is evaluated as: $\rho^{ij} = \text{sign}((\mathcal{A}_p^i - \mathcal{A}_m^i)(\mathcal{A}_p^j - \mathcal{A}_m^j))$

400 These are added up to construct the covariance matrices. When we vary the PDF parameters,
 401 the normalizations in the central and high $|\eta|$ bins change in the opposite direction which
 402 results in negative correlations in the extracted asymmetries between the central and high $|\eta|$
 403 bins.

404 The PDF uncertainty is estimated to be about 10% of the total experimental uncertainty. The
 405 remaining sources of systematic errors have even smaller contribution than the PDF, and many
 406 of them are negligible.

407 6.2.4 Drell-Yan background

408 The $Z/\gamma^* \rightarrow \mu^+\mu^-$ events in the Drell-Yan control region are used to check the Drell-Yan
 409 normalization. This is done in several bins of dimuon invariant mass regions: [15, 30, 40, 60,
 410 120, 150, inf] GeV. The $Z/\gamma^* \rightarrow \mu^+\mu^-$ MC simulation in each bin is compared to the data
 411 yields after correcting the MC for data/MC difference in PU, Z boson q_T , \cancel{E}_T modeling, and
 412 efficiencies. After correcting for the detector bias and physics mis-modeling, the MC simulation
 413 describes the data well, as shown in Figure 2 for dimuon invariant mass between [60, 120] GeV.
 414 The data yield in this bin is about 3% higher than the predictions from the NNLO cross section
 415 as calculated by FEWZ 3.0 [31]. This 3% is summed in quadrature with the PDF uncertainty
 416 and the sum is treated as the total uncertainty in predicting the $Z/\gamma^* \rightarrow \mu^+\mu^-$ yields using MC
 417 simulation, shown by the yellow band in Figure 2.

418 The ratio of data to MC of the $Z/\gamma^* \rightarrow \mu^+\mu^-$ event yields are used to rescale the MC prediction
 419 of Drell-Yan background based on the generated dimuon invariant mass. We take the shift on
 420 the raw charge asymmetry with and without this rescaling as the systematic uncertainty. This
 421 and the PDF uncertainty on the $Z/\gamma^* \rightarrow \mu^+\mu^-$ yields are considered as systematic uncertainty
 422 due to ‘‘Drell-Yan background normalization’’. This uncertainty is almost negligible at central
 423 $|\eta|$ bins and increases in the forward $|\eta|$ bins. This is because the Drell-Yan background is
 424 significantly larger in the forward region due to the fact that the ‘‘Drell-Yan veto’’ has lower
 425 efficiency due to detector coverage. The systematic uncertainty in the Drell-Yan background is
 426 assumed to have 100% correlation from bin to bin.

427 6.2.5 \vec{E}_T modeling

428 To evaluate the systematic uncertainty due to the Φ -modulation of \vec{E}_T , the correction for the
 429 Φ -modulation is removed and the shift in the raw charge asymmetry is taken as the systematic
 430 uncertainty.

431 The hadronic recoil correction changes the shape of the \cancel{E}_T distribution of all MC samples. To
 432 calculate the systematic error from this source, the average recoil and resolution parameters are
 433 smeared within their uncertainties, taking into account the correlations between them. This is

434 done 400 times and the RMS of the resulting \mathcal{A}^{raw} distribution is taken as systematic uncertainty
 435 and bin-to-bin correlations are calculated.

436 6.2.6 Pile-up

437 Pile-up can affect the \cancel{E}_T shapes. To estimate the effect of mis-modeling of PU in the simulation,
 438 the minimum bias cross-section is varied by $\pm 5\%$ and the PU distributions expected in data are
 439 re-generated. The MC simulation is then reweighted to match to data and the resulting shift
 440 in \mathcal{A}^{raw} is treated as systematic uncertainty from PU. PU affects the \cancel{E}_T shapes for all muon
 441 pseudorapidity bins in the same direction with a correlation of 100%. However, the resulting
 442 asymmetry could be either positively or negatively 100% correlated from bin to bin.

443 6.2.7 Integrated luminosity

444 The $Z/\gamma^* \rightarrow \tau^+\tau^-$ and $t\bar{t}$ backgrounds are normalized to the data luminosity after correcting
 445 for the muon efficiency difference between data and MC simulation. The uncertainty on the
 446 integrated luminosity is about 2.2%. The normalization of all the MC backgrounds is varied by
 447 $\pm 2.2\%$, and the resulting maximum shift in \mathcal{A}^{raw} is taken as systematic uncertainty from un-
 448 certainties in the determination of the luminosity. The bin-to-bin correlations in the measured
 449 asymmetries are +100%.

450 6.2.8 $t\bar{t}$ and $W \rightarrow \tau\nu$ background

451 An additional 15% is assigned as the uncertainty in the theoretical prediction [26] of the $t\bar{t}$ cross
 452 section. This has a similar effect as the uncertainty on integrated luminosity and the bin-to-bin
 453 correlation in the extracted asymmetry is assumed to be 100%.

454 The $W \rightarrow \tau\nu$ background is normalized to the $W \rightarrow \mu\nu$ yields in data with a ratio obtained
 455 from a MC simulation. This ratio is largely determined by the branching fraction of τ decaying
 456 to μ . A 2% uncertainty is assigned to the $W \rightarrow \tau\nu$ to $W \rightarrow \mu\nu$ ratio [34]. Here, the bin-to-bin
 457 correlations in the measured asymmetries are +100%.

458 6.2.9 W boson q_T modeling

459 To improve the agreement between data and simulation, the W boson q_T spectrum is reweighted
 460 using weight factors which are the ratios of the distribution of boson q_T for $Z/\gamma^* \rightarrow \mu^+\mu^-$
 461 events in data and MC simulation. Here we make the assumption that the scale factors to cor-
 462 rect the boson q_T distribution in MC simulation to match the data are the same for W and Z
 463 events. This assumption is tested using two different sets of MC simulations: one from the
 464 POWHEG event generator and the other from MADGRAPH [35]. Here, MADGRAPH is
 465 treated as the "data", and the ratio of Z boson q_T between the MADGRAPH simulation and
 466 the POWHEG simulation is compared to the same ratio in simulated W events. The maximum
 467 variation of this double ratio is within $\pm 10\%$. This double ratio is parametrized using an empir-
 468 ical function to smooth the statistical fluctuations, and additional weights are obtained using
 469 the fitted function. Here we reweight the POWHEG simulation to be close to MADGRAPH
 470 simulation and measure the asymmetry again. The deviation of \mathcal{A}^{raw} is taken as the systematic
 471 uncertainty due to mis-modeling of W boson q_T . The default boson q_T reweighting which is
 472 applied is based on the POWHEG simulation.

473 6.3 Total systematic uncertainty

474 Table 2 summarizes the total systematic uncertainty in each $|\eta|$ bin. For comparison, the sta-
 475 tistical uncertainty in each $|\eta|$ bin is also shown in the same table. The dominant systematic

476 uncertainty is from uncertainties in the muon efficiencies, QCD background, and muon scale
 477 correction. The correlation matrix of systematic uncertainty between different $|\eta|$ bins is sum-
 478 marized in Table 3. The correlations between different $|\eta|$ bins are small. The maximum corre-
 479 lation between different $|\eta|$ bins is about 13% and 3.5% for muon p_T threshold of 25 GeV and
 35 GeV, respectively.

Table 2: Total systematic uncertainty in each $|\eta|$ bin. The statistical uncertainty in each $|\eta|$ bin
 is also shown for comparison. A detailed description of each systematic uncertainty is given in
 the text. The units are in percent.

$ \eta $ bin	0.0-0.2	0.2-0.4	0.4-0.6	0.6-0.8	0.8-1.0	1.0-1.2	1.2-1.4	1.4-1.6	1.6-1.85	1.85-2.1	2.1-2.4
$p_T > 25$ GeV											
Stat. unc.	0.096	0.098	0.094	0.093	0.098	0.099	0.099	0.099	0.093	0.094	0.106
Efficiency	0.111	0.133	0.121	0.122	0.170	0.175	0.170	0.168	0.165	0.175	0.268
QCD +/-	0.120	0.113	0.110	0.105	0.102	0.103	0.097	0.104	0.108	0.094	0.183
QCD shape	0.070	0.065	0.065	0.067	0.068	0.069	0.078	0.082	0.092	0.083	0.087
Muon scale	0.045	0.050	0.050	0.049	0.051	0.054	0.054	0.058	0.054	0.054	0.055
PDF	0.028	0.026	0.023	0.025	0.018	0.020	0.027	0.031	0.042	0.050	0.069
Drell-Yan bkg.	0.002	0.001	0.002	0.003	0.000	0.007	0.001	0.013	0.019	0.038	0.046
$\cancel{E}_T \Phi$ modul.	0.011	0.009	0.033	0.012	0.029	0.034	0.044	0.045	0.055	0.049	0.038
Recoil	0.003	0.003	0.003	0.003	0.003	0.003	0.003	0.003	0.003	0.004	0.003
PU	0.017	0.013	0.011	0.005	0.014	0.025	0.022	0.031	0.019	0.028	0.000
Luminosity	0.002	0.003	0.004	0.004	0.006	0.009	0.012	0.017	0.024	0.033	0.040
$t\bar{t}$ bkg.	0.012	0.013	0.012	0.012	0.011	0.011	0.010	0.009	0.008	0.007	0.005
$W \rightarrow \tau\nu$ bkg.	0.026	0.026	0.026	0.026	0.026	0.025	0.025	0.025	0.025	0.025	0.024
$W q_T$	0.003	0.004	0.004	0.005	0.008	0.011	0.008	0.009	0.006	0.003	0.000
Total syst. unc.	0.189	0.197	0.190	0.186	0.221	0.229	0.227	0.233	0.239	0.241	0.355
Total unc.	0.212	0.220	0.212	0.208	0.242	0.249	0.248	0.253	0.256	0.259	0.371
$p_T > 35$ GeV											
Stat. unc.	0.116	0.119	0.114	0.114	0.124	0.121	0.123	0.123	0.118	0.123	0.141
Efficiency	0.120	0.138	0.116	0.107	0.159	0.164	0.171	0.176	0.186	0.194	0.325
QCD +/-	0.151	0.138	0.135	0.128	0.133	0.118	0.116	0.122	0.137	0.120	0.168
QCD shape	0.030	0.025	0.017	0.023	0.024	0.022	0.018	0.017	0.031	0.031	0.037
Muon scale	0.122	0.135	0.134	0.141	0.146	0.154	0.162	0.170	0.161	0.172	0.189
PDF	0.008	0.008	0.007	0.011	0.012	0.010	0.017	0.022	0.031	0.040	0.058
Drell-Yan bkg.	0.010	0.009	0.009	0.003	0.006	0.010	0.008	0.009	0.009	0.020	0.040
$\cancel{E}_T \Phi$ modul.	0.002	0.009	0.010	0.003	0.008	0.028	0.037	0.035	0.022	0.022	0.001
Recoil	0.005	0.006	0.005	0.004	0.005	0.004	0.005	0.004	0.004	0.006	0.008
PU	0.015	0.003	0.005	0.018	0.019	0.002	0.007	0.003	0.013	0.014	0.032
Luminosity	0.001	0.002	0.000	0.000	0.000	0.001	0.004	0.010	0.016	0.025	0.039
$t\bar{t}$ bkg.	0.011	0.013	0.012	0.011	0.011	0.010	0.010	0.009	0.007	0.006	0.005
$W \rightarrow \tau\nu$ bkg.	0.013	0.012	0.013	0.012	0.012	0.012	0.011	0.012	0.011	0.011	0.011
$W q_T$	0.004	0.002	0.004	0.004	0.007	0.005	0.006	0.009	0.009	0.001	0.014
Total syst. unc.	0.232	0.240	0.225	0.221	0.257	0.258	0.267	0.277	0.287	0.294	0.423
Total unc.	0.260	0.268	0.252	0.248	0.285	0.285	0.294	0.303	0.311	0.318	0.446

480

481 7 Results and discussion

482 The measured asymmetries (\mathcal{A}) after all corrections are shown in Figure 7 and summarized in
 483 Table 4. Both statistical and systematic uncertainties are included. The asymmetries are com-
 484 pared to several PDF models. The theoretical predictions are obtained using FEWZ 3.0 [31] MC
 485 interfaced with CT10 [3], NNPDF2.3 [33], HERA1.5 [36], MSTW2008 [2], and MSTW2008-
 486 CPDEUT [14] NLO PDF models. The numerical values of the theoretical predictions are also
 487 shown in Table 4. The CT10 PDF and HERA1.5 parametrization are in good agreement with
 488 the data. The NNPDF2.3 includes the previous CMS electron charge asymmetry result [10]

Table 3: Correlation matrix of systematic uncertainties between different $|\eta|$ bins. The units are in percent.

$ \eta $ bin	0.0-0.2	0.2-0.4	0.4-0.6	0.6-0.8	0.8-1.0	1.0-1.2	1.2-1.4	1.4-1.6	1.6-1.85	1.85-2.1	2.1-2.4
$p_T > 25$ GeV											
0.00-0.20	100.0	4.8	5.5	4.6	4.4	4.4	4.2	4.3	4.0	3.7	1.2
0.20-0.40		100.0	5.0	4.1	3.8	3.8	3.6	3.7	3.3	3.0	0.8
0.40-0.60			100.0	4.9	5.5	5.7	6.1	6.1	6.2	5.5	2.2
0.60-0.80				100.0	4.1	4.1	4.0	4.1	4.3	3.9	1.8
0.80-1.00					100.0	5.0	5.4	5.6	5.8	5.5	2.4
1.00-1.20						100.0	6.4	7.1	7.1	7.3	3.3
1.20-1.40							100.0	8.4	8.7	8.7	4.3
1.40-1.60								100.0	10.0	10.8	5.7
1.60-1.85									100.0	12.8	7.5
1.85-2.10										100.0	9.5
2.10-2.40											100.0
$p_T > 35$ GeV											
0.00-0.20	100.0	0.9	0.9	1.2	1.1	0.6	0.6	0.3	0.5	0.4	0.3
0.20-0.40		100.0	0.6	0.7	0.6	0.2	-0.0	-0.3	-0.1	-0.2	-0.1
0.40-0.60			100.0	1.0	1.0	1.2	1.3	1.0	0.8	0.6	0.1
0.60-0.80				100.0	1.4	0.8	0.9	0.8	1.0	1.1	1.0
0.80-1.00					100.0	1.1	1.2	1.0	1.2	1.1	0.7
1.00-1.20						100.0	2.2	1.9	1.4	1.3	0.1
1.20-1.40							100.0	2.5	2.0	1.9	0.5
1.40-1.60								100.0	2.4	2.6	1.3
1.60-1.85									100.0	3.1	2.2
1.85-2.10										100.0	3.5
2.10-2.40											100.0

489 and other LHC experimental measurements, and it also shows good agreement with the data.
 490 The MSTW2008 PDF parametrization shows poor agreement with the data. The more recent
 491 MSTW2008CPDEUT PDF set is a variant of the MSTW2008 PDF set with a more flexible input
 492 parametrization and deuteron corrections [14]. This modification has significantly improved
 493 the agreement with the CMS data without including the LHC data, as shown in Figure 7. Since
 494 the per-bin experimental total uncertainty is significantly smaller than the present uncertainty
 495 in the PDF, this measurement can be used to improve understanding of different PDF predic-
 496 tions and to reduce the PDF uncertainty for different parton flavors.

497 Figure 8 shows a comparison of this result to previous CMS lepton charge asymmetry measure-
 498 ments. For most of the data points, the agreement is within one standard derivation. Note that
 499 in the previous lepton charge asymmetry results [8] [11], the central values were not corrected
 500 for any difference in efficiency between positive and negative muons (which is done for this re-
 501 sult), but the statistical uncertainty in the determination of the efficiency ratio was included in
 502 the total systematic error. The data sample used in the previous CMS muon charge asymmetry
 503 measurement [11] is included in the dataset used here. Therefore, this result supersedes this
 504 previous measurement. The electron charge asymmetry extracted from part of the 2011 CMS
 505 data [10] uses a statistically independent data sample from this result. A combination of both
 506 results can potentially improve the constraints to PDF global fits. The correlation between the
 507 electron charge asymmetry and this result is expected to be small. The completely correlated
 508 systematic sources are due to luminosity measurement, $t\bar{t}$ background, $W \rightarrow \tau\nu$ background,
 509 and PDF uncertainty.

510 The theoretical predictions for the lepton charge asymmetry are given for the kinematic region
 511 specified by the lepton p_T threshold. The acceptance is affected by the modeling of the W boson

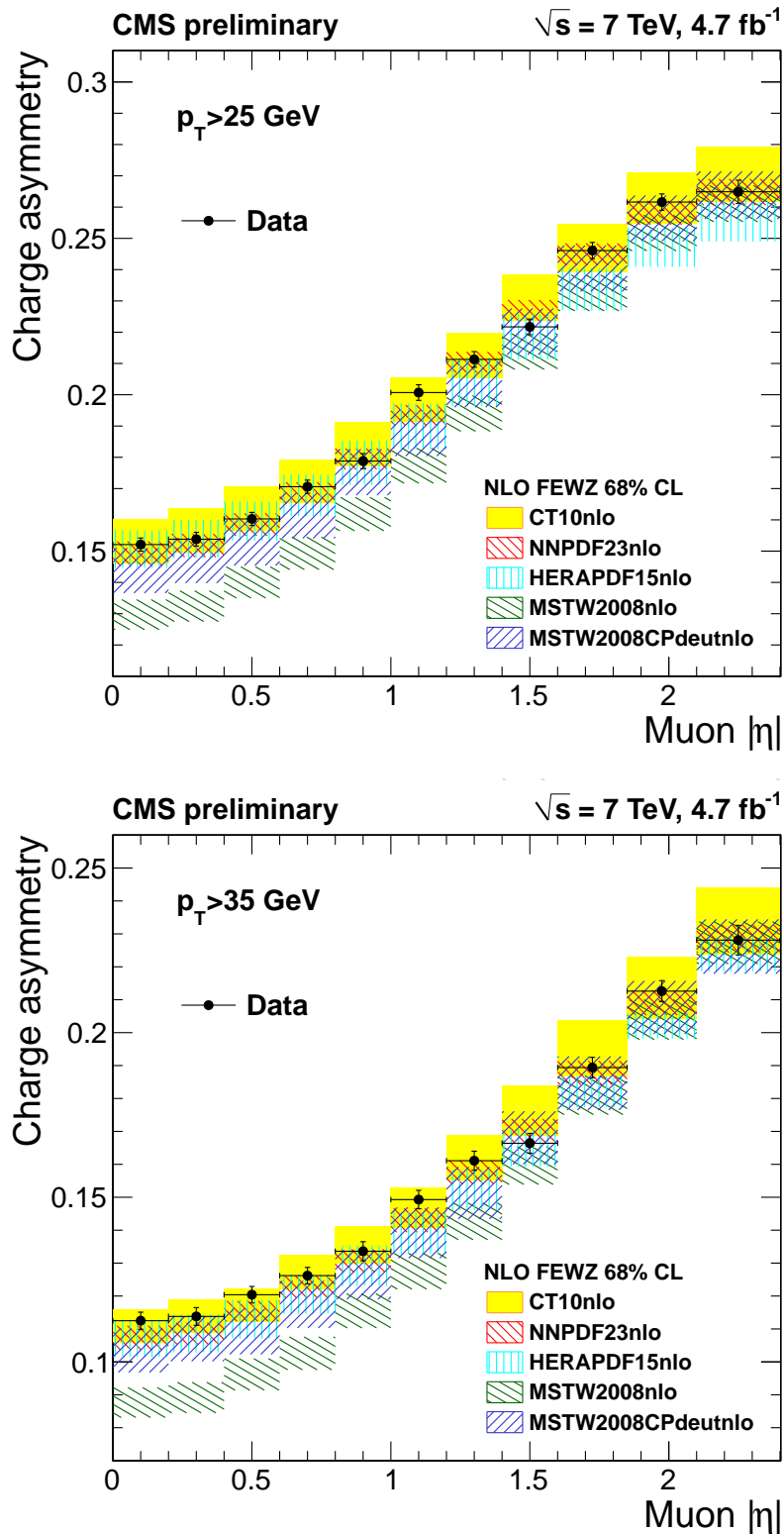


Figure 7: Comparison of the measured muon charge asymmetries to predictions with CT10 [3], NNPDF2.3 [33], HERAPDF1.5 [36], MSTW2008 [2], and MSTW2008CP_{DEUT} [14] NLO PDF models. Results for muon $p_T > 25 \text{ GeV}$ and muon $p_T > 35 \text{ GeV}$ are shown on the top and bottom panels, respectively. The error bars include both statistical and systematic uncertainties. The PDF uncertainty band corresponds to 68% confidence level (C.L.). The data points are shown at the center of each pseudorapidity bin. The theoretical predictions are calculated using the FEWZ 3.0 [31] MC.

Table 4: Summary of the final results for muon charge asymmetry (\mathcal{A}). The first uncertainty is statistical and the second is systematic. The theoretical predictions are obtained using FEWZ 3.0 [31] MC interfaced with CT10 [3], NNPDF2.3 [33], HERAPDF1.5 [36], and MSTW2008-CPDEUT [14] NLO PDF models. The PDF uncertainty is at 68% C.L. For each pseudorapidity bin the theoretical prediction is calculated using the averaged differential cross sections for positively and negatively charged leptons respectively. The units are in percent.

$ \eta $	$\mathcal{A} (\pm\text{stat.}\pm\text{syst.})$	CT10	NNPDF2.3	HERAPDF1.5	MSTW2008CPDEUT
$p_T > 25 \text{ GeV}$					
0.00-0.20	$15.21 \pm 0.10 \pm 0.19$	$15.29^{+0.74}_{-0.68}$	14.92 ± 0.39	$15.29^{+0.37}_{-0.82}$	$14.35^{+0.75}_{-0.69}$
0.20-0.40	$15.38 \pm 0.10 \pm 0.20$	$15.63^{+0.73}_{-0.69}$	15.18 ± 0.37	$15.59^{+0.41}_{-0.80}$	$14.67^{+0.75}_{-0.69}$
0.40-0.60	$16.03 \pm 0.09 \pm 0.19$	$16.36^{+0.71}_{-0.70}$	15.85 ± 0.36	$16.18^{+0.41}_{-0.85}$	$15.24^{+0.75}_{-0.70}$
0.60-0.80	$17.06 \pm 0.09 \pm 0.19$	$17.25^{+0.68}_{-0.71}$	16.86 ± 0.34	$17.01^{+0.44}_{-0.90}$	$16.12^{+0.74}_{-0.71}$
0.80-1.00	$17.88 \pm 0.10 \pm 0.22$	$18.47^{+0.66}_{-0.74}$	17.95 ± 0.33	$18.04^{+0.49}_{-0.92}$	$17.52^{+0.74}_{-0.73}$
1.00-1.20	$20.07 \pm 0.10 \pm 0.23$	$19.89^{+0.64}_{-0.76}$	19.34 ± 0.33	$19.14^{+0.58}_{-0.88}$	$18.78^{+0.73}_{-0.74}$
1.20-1.40	$21.13 \pm 0.10 \pm 0.23$	$21.35^{+0.63}_{-0.80}$	21.04 ± 0.33	$20.58^{+0.60}_{-0.94}$	$20.36^{+0.72}_{-0.76}$
1.40-1.60	$22.17 \pm 0.10 \pm 0.23$	$23.21^{+0.64}_{-0.84}$	22.69 ± 0.34	$21.91^{+0.66}_{-0.79}$	$22.06^{+0.70}_{-0.78}$
1.60-1.85	$24.61 \pm 0.09 \pm 0.24$	$24.81^{+0.65}_{-0.89}$	24.49 ± 0.35	$23.36^{+0.68}_{-0.66}$	$24.09^{+0.68}_{-0.79}$
1.85-2.10	$26.16 \pm 0.09 \pm 0.24$	$26.43^{+0.67}_{-0.95}$	25.82 ± 0.38	$24.63^{+0.71}_{-0.54}$	$25.72^{+0.65}_{-0.81}$
2.10-2.40	$26.49 \pm 0.11 \pm 0.36$	$27.19^{+0.74}_{-1.03}$	26.48 ± 0.42	$25.40^{+0.81}_{-0.50}$	$26.49^{+0.65}_{-0.87}$
$p_T > 35 \text{ GeV}$					
0.00-0.20	$11.25 \pm 0.12 \pm 0.23$	$11.07^{+0.52}_{-0.48}$	10.73 ± 0.37	$10.92^{+0.36}_{-0.77}$	$10.35^{+0.67}_{-0.67}$
0.20-0.40	$11.38 \pm 0.12 \pm 0.24$	$11.36^{+0.52}_{-0.49}$	10.86 ± 0.33	$11.06^{+0.38}_{-0.77}$	$10.70^{+0.68}_{-0.68}$
0.40-0.60	$12.04 \pm 0.11 \pm 0.23$	$11.71^{+0.52}_{-0.50}$	11.54 ± 0.31	$11.50^{+0.39}_{-0.79}$	$10.92^{+0.70}_{-0.69}$
0.60-0.80	$12.62 \pm 0.11 \pm 0.22$	$12.72^{+0.52}_{-0.53}$	12.28 ± 0.33	$12.22^{+0.44}_{-0.76}$	$11.74^{+0.72}_{-0.71}$
0.80-1.00	$13.36 \pm 0.12 \pm 0.26$	$13.58^{+0.55}_{-0.58}$	13.07 ± 0.35	$13.08^{+0.46}_{-0.77}$	$12.64^{+0.75}_{-0.74}$
1.00-1.20	$14.93 \pm 0.12 \pm 0.26$	$14.72^{+0.59}_{-0.64}$	14.30 ± 0.36	$14.10^{+0.45}_{-0.82}$	$13.92^{+0.77}_{-0.77}$
1.20-1.40	$16.11 \pm 0.12 \pm 0.27$	$16.24^{+0.64}_{-0.73}$	15.76 ± 0.36	$15.35^{+0.48}_{-0.73}$	$15.13^{+0.79}_{-0.79}$
1.40-1.60	$16.64 \pm 0.12 \pm 0.28$	$17.69^{+0.70}_{-0.83}$	17.02 ± 0.36	$16.60^{+0.47}_{-0.67}$	$16.82^{+0.79}_{-0.82}$
1.60-1.85	$18.94 \pm 0.12 \pm 0.29$	$19.63^{+0.76}_{-0.94}$	18.78 ± 0.36	$18.22^{+0.45}_{-0.48}$	$18.51^{+0.77}_{-0.86}$
1.85-2.10	$21.26 \pm 0.12 \pm 0.29$	$21.48^{+0.82}_{-1.06}$	20.91 ± 0.38	$20.11^{+0.48}_{-0.29}$	$20.86^{+0.71}_{-0.90}$
2.10-2.40	$22.81 \pm 0.14 \pm 0.42$	$23.55^{+0.86}_{-1.17}$	22.85 ± 0.42	$22.23^{+0.67}_{-0.37}$	$22.78^{+0.66}_{-0.99}$

512 p_T which affects the prediction for the charge asymmetry. However, the effect on W^+ and W^- is
513 largely correlated in the same direction. Therefore, the impact on the lepton charge asymmetry
514 measurement cancels to first order. Figure 9 shows the comparison of these results to CT10NLO
515 predictions based on FEWZ 3.0 and RESBOS [37–39]. RESBOS does a resummation in boson
516 q_T at approximate next-to-next-to-leading logarithm which yields a more realistic description
517 of boson q_T than a fixed-order calculation such as FEWZ 3.0. However, the difference between
518 FEWZ 3.0 and RESBOS is negligible, and our measurement is not able to be sensitive to the
519 small difference between a fixed-order calculation and a boson q_T resummed prediction.

520 8 Summary

521 In summary, the $W \rightarrow \mu\nu$ lepton charge asymmetry is measured using a data sample corre-
522 sponding to an integrated luminosity of 4.7 fb^{-1} collected with the CMS detector at the LHC (a
523 sample of more than 20M $W \rightarrow \mu\nu$ events). The asymmetry is measured in 11 bins in absolute
524 muon pseudorapidity for two different muon p_T thresholds: 25 GeV and 35 GeV. Compared

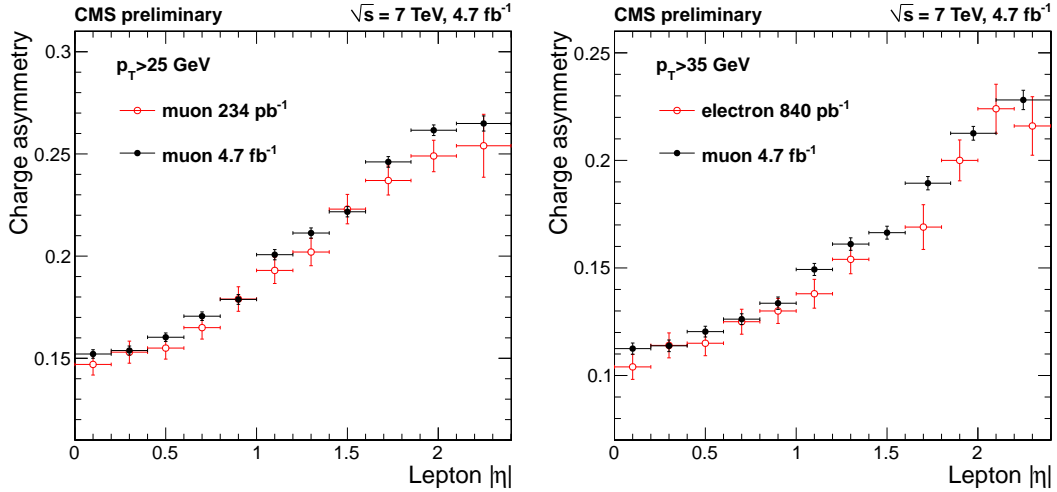


Figure 8: Comparison of this measurement to previous CMS lepton charge asymmetry results [10] [11]. Results are shown for muon $p_T > 25$ GeV (left) and muon $p_T > 35$ GeV (right).

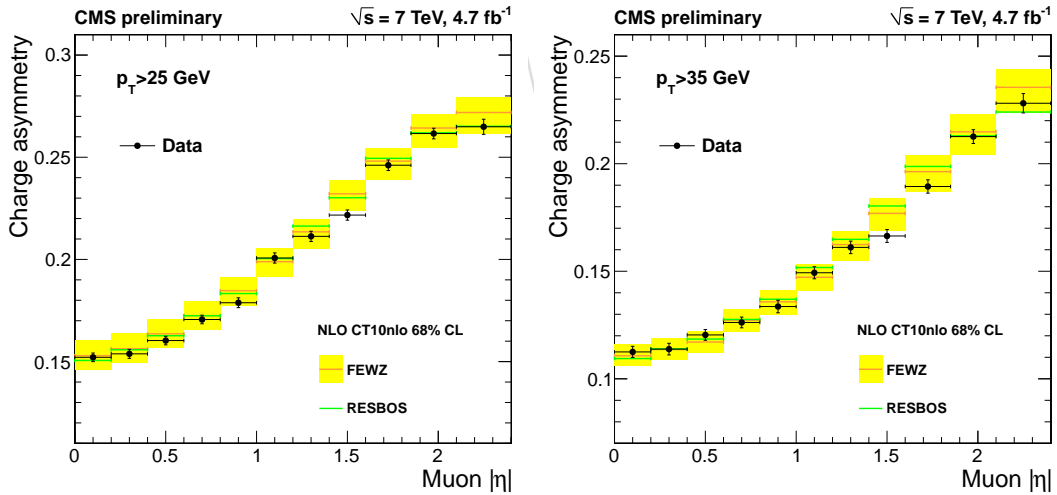


Figure 9: Comparison of the measured muon charge asymmetry to theoretical predictions based on FEWZ 3.0 and RESBOS MC calculations. The CT10 NLO PDF is used in both predictions. Results are shown for muon $p_T > 25$ GeV (left) and muon $p_T > 35$ GeV (right).

525 to the previous CMS measurement, this measurement significantly reduces both the statisti-
526 cal and systematic uncertainties. The total uncertainty per bin is 0.2-0.4%. The data are in
527 good agreement with the CT10, NNPDF2.3, and HERA1.5 PDF parametrization. The data
528 are in poor agreement with the MSTW2008 parametrization, however the agreement has been
529 significantly improved with the MSTW2008CPDEUT PDF set. The experimental errors are
530 smaller than PDF uncertainties of the predictions. Therefore, this measurement can be used to
531 significantly improve future PDFs.

532 Acknowledgments

533 We congratulate our colleagues in the CERN accelerator departments for the excellent perfor-
534 mance of the LHC and thank the technical and administrative staffs at CERN and at other CMS
535 institutes for their contributions to the success of the CMS effort. In addition, we gratefully ac-
536 knowledge the computing centres and personnel of the Worldwide LHC Computing Grid for
537 delivering so effectively the computing infrastructure essential to our analyses. Finally, we ac-
538 knowledge the enduring support for the construction and operation of the LHC and the CMS
539 detector provided by the following funding agencies: BMWF and FWF (Austria); FNRS and
540 FWO (Belgium); CNPq, CAPES, FAPERJ, and FAPESP (Brazil); MEYS (Bulgaria); CERN; CAS,
541 MoST, and NSFC (China); COLCIENCIAS (Colombia); MSES (Croatia); RPF (Cyprus); MoER,
542 SF0690030s09 and ERDF (Estonia); Academy of Finland, MEC, and HIP (Finland); CEA and
543 CNRS/IN2P3 (France); BMBF, DFG, and HGF (Germany); GSRT (Greece); OTKA and NKTH
544 (Hungary); DAE and DST (India); IPM (Iran); SFI (Ireland); INFN (Italy); NRF and WCU (Re-
545 public of Korea); LAS (Lithuania); CINVESTAV, CONACYT, SEP, and UASLP-FAI (Mexico);
546 MSI (New Zealand); PAEC (Pakistan); MSHE and NSC (Poland); FCT (Portugal); JINR (Arme-
547 nia, Belarus, Georgia, Ukraine, Uzbekistan); MON, RosAtom, RAS and RFBR (Russia); MSTP
548 (Serbia); SEIDI and CPAN (Spain); Swiss Funding Agencies (Switzerland); NSC (Taipei); ThEP-
549 Center, IPST and NSTDA (Thailand); TUBITAK and TAEK (Turkey); NASU (Ukraine); STFC
550 (United Kingdom); DOE and NSF (USA).

551 Individuals have received support from the Marie-Curie programme and the European Re-
552 search Council (European Union); the Leventis Foundation; the A. P. Sloan Foundation; the
553 Alexander von Humboldt Foundation; the Belgian Federal Science Policy Office; the Fonds
554 pour la Formation à la Recherche dans l'Industrie et dans l'Agriculture (FRIA-Belgium); the
555 Agentschap voor Innovatie door Wetenschap en Technologie (IWT-Belgium); the Ministry of
556 Education, Youth and Sports (MEYS) of Czech Republic; the Council of Science and Industrial
557 Research, India; the Compagnia di San Paolo (Torino); and the HOMING PLUS programme of
558 Foundation for Polish Science, cofinanced from European Union, Regional Development Fund.

559 References

- 560 [1] CMS Collaboration, "Measurements of Inclusive W and Z Cross Sections in pp Collisions
561 at $\sqrt{s} = 7$ TeV", *JHEP* **1101** (2011) 080, doi:10.1007/JHEP01(2011)080,
562 arXiv:1012.2466.
- 563 [2] A. D. Martin, W. J. Stirling, R. S. Thorne, and G. Watt, "Parton distributions for the LHC",
564 *Eur. Phys. J.* **C63** (2009) 189–285, doi:10.1140/epjc/s10052-009-1072-5,
565 arXiv:0901.0002.
- 566 [3] H.-L. Lai et al., "New parton distributions for collider physics", *Phys. Rev.* **D82** (2010)
567 074024, doi:10.1103/PhysRevD.82.074024, arXiv:1007.2241.

- 568 [4] J. D. Björken and E. A. Paschos, “Inelastic electron proton and gamma proton scattering,
569 and the structure of the nucleon”, *Phys. Rev.* **185** (1969) 1975–1982,
570 doi:10.1103/PhysRev.185.1975.
- 571 [5] CDF Collaboration, “Direct measurement of the W production charge asymmetry in p \bar{p}
572 Collisions at $\sqrt{s} = 1.96$ TeV”, *Phys. Rev. Lett.* **102** (2009) 181801,
573 doi:10.1103/PhysRevLett.102.181801, arXiv:0901.2169.
- 574 [6] D0 Collaboration, “Measurement of the electron charge asymmetry in
575 p $\bar{p} \rightarrow W + X \rightarrow e\nu + X$ events at $\sqrt{s} = 1.96$ TeV”, *Phys. Rev. Lett.* **101** (2008) 211801,
576 doi:10.1103/PhysRevLett.101.211801, arXiv:0807.3367.
- 577 [7] ATLAS Collaboration, “Measurement of the Muon Charge Asymmetry from W Bosons
578 Produced in pp Collisions at $\sqrt{s} = 7$ TeV with the ATLAS detector”, *Phys.Lett. B* **701**
579 (2011) 31, doi:10.1016/j.physletb.2011.05.024, arXiv:1103.2929v1.
- 580 [8] CMS Collaboration, “Measurement of the lepton charge asymmetry in inclusive W
581 production in pp collisions at $\sqrt{s} = 7$ TeV”, *JHEP* **04** (2011) 050,
582 doi:10.1007/JHEP04(2011)050, arXiv:1103.3470v1.
- 583 [9] LHCb Collaboration, “Inclusive W and Z production in the forward region at $\sqrt{s} = 7$
584 TeV”, *JHEP* **06** (2012) 058, doi:10.1007/JHEP06(2012)058,
585 arXiv:1204.1620v3.
- 586 [10] CMS Collaboration, “Measurement of the electron charge asymmetry in inclusive W
587 production in pp collisions at $\sqrt{s} = 7$ TeV”, *Phys.Rev.Lett.* **109** (2012) 111806,
588 doi:10.1103/PhysRevLett.109.111806, arXiv:1206.2598.
- 589 [11] CMS Collaboration, “Measurement of the muon charge asymmetry in inclusive W
590 production in pp collisions at $\sqrt{s} = 7$ TeV”, *CMS PAS EWK-11-005* (2011).
- 591 [12] R. D. Ball et al., “Reweightings and Unweightings of Parton Distributions and the LHC W
592 lepton asymmetry data”, *Nucl.Phys.* **B855** (2012) 608–638,
593 doi:10.1016/j.nuclphysb.2011.10.018, arXiv:1108.1758.
- 594 [13] S. Alekhin, J. Bluemlein, and S. Moch, “PDF fit in the fixed-flavor-number scheme”,
595 arXiv:hep-ph/1202.4642.
- 596 [14] A. Martin et al., “Extended Parameterisations for MSTW PDFs and their effect on Lepton
597 Charge Asymmetry from W Decays”, *Eur.Phys.J.* **C73** (2013) 2318,
598 doi:10.1140/epjc/s10052-013-2318-9, arXiv:1211.1215.
- 599 [15] CMS Collaboration, “The CMS experiment at the CERN LHC”, *JINST* **03** (2008) S08004,
600 doi:10.1088/1748-0221/3/08/S08004.
- 601 [16] CMS Collaboration, “Particle-flow commissioning with muons and electrons from J/ Ψ ,
602 and W events at 7 TeV”, *CMS PAS PFT-2010-003* (2010).
- 603 [17] S. Frixione, P. Nason, and C. Oleari, “Matching NLO QCD computations with parton
604 shower simulations: the POWHEG method”, *JHEP* **11** (2007) 070,
605 doi:10.1088/1126-6708/2007/11/070, arXiv:0709.2092.
- 606 [18] Z. Was, “TAUOLA the library for tau lepton decay, and KKMC / KORALB / KORALZ
607 /... status report”, *Nucl.Phys.Proc.Suppl.* **98** (2001) 96–102,
608 doi:10.1016/S0920-5632(01)01200-2, arXiv:hep-ph/0011305.

- 609 [19] T. Sjöstrand, S. Mrenna, and P. Z. Skands, “PYTHIA 6.4 physics and manual”, *JHEP* **05**
610 (2006) 026, doi:10.1088/1126-6708/2006/05/026, arXiv:hep-ph/0603175.
- 611 [20] J. Pumplin et al., “New generation of parton distributions with uncertainties from global
612 QCD analysis”, *JHEP* **07** (2002) 012, doi:10.1088/1126-6708/2002/07/012,
613 arXiv:hep-ph/0201195.
- 614 [21] GEANT4 Collaboration, “GEANT4: a simulation toolkit”, *Nucl. Instrum. Meth.* **A506**
615 (2003) 250–303, doi:10.1016/S0168-9002(03)01368-8.
- 616 [22] CMS Collaboration, “Performance of muon identification in pp collisions at $\sqrt{s}=7$ TeV”,
617 *CMS PAS MUO-10-002* (2010).
- 618 [23] CMS Collaboration, “Performance of muon identification in pp collisions at $\sqrt{s}=7$ TeV”,
619 *JINST* **7** (2012) P10002, doi:10.1088/1748-0221/7/10/P10002.
- 620 [24] A. Bodek, A. van Dyne, J.Y. Han, W. Sakumoto, and A. Strelnikov, “Extracting muon
621 momentum scale corrections for hadron collider experiments”, *Eur. Phys. J. C* **72**, 10
622 (2012).
- 623 [25] R. Barlow and C. Beeston, “Fitting using finite Monte Carlo samples”, *Comp. Phys.*
624 *Comm.* **77** (1993) 219–228.
- 625 [26] J. M. Campbell and R. K. Ellis, “Radiative corrections to $Zb\bar{b}$ production”, *Phys. Rev.* **D62**
626 (2000) 114012, doi:10.1103/PhysRevD.62.114012, arXiv:hep-ph/0006304.
- 627 [27] CDF Collaboration, “First run II measurement of the W boson mass at the Fermilab
628 Tevatron”, *Phys. Rev. D* **77** (2008) 112001, doi:10.1103/PhysRevD.77.112001.
- 629 [28] D0 Collaboration, “A Novel method for modeling the recoil in W boson events at hadron
630 collider”, *Nucl.Instrum.Meth.* **A609** (2009) 250–262,
631 doi:10.1016/j.nima.2009.08.056, arXiv:0907.3713.
- 632 [29] CMS Collaboration, “CMS MET performance in events containing electroweak bosons
633 from pp Collisions at $\sqrt{s}=7$ TeV”, *CMS PAS JME-2010-005* (2010).
- 634 [30] M. Cacciari, G. P. Salam, and G. Soyez, “The anti- k_t jet clustering algorithm”, *JHEP* **04**
635 (2008) 063, doi:10.1088/1126-6708/2008/04/063, arXiv:0802.1189.
- 636 [31] Y. Li and F. Petriello, “Combining QCD and electroweak corrections to dilepton
637 production in FEWZ”, arXiv:1208.5967.
- 638 [32] M. Botje et al., “The PDF4LHC Working Group Interim Recommendations”,
639 arXiv:1101.0538.
- 640 [33] R. D. Ball et al., “Parton distributions with LHC data”, *Nucl.Phys.* **B867** (2013) 244–289,
641 doi:10.1016/j.nuclphysb.2012.10.003, arXiv:1207.1303.
- 642 [34] Particle Data Group Collaboration, “Review of Particle Physics”, *Phys. Rev. D* **86** (2012)
643 010001, doi:10.1103/PhysRevD.86.010001.
- 644 [35] J. Alwall et al., “MadGraph 5 : Going Beyond”, *JHEP* **1106** (2011) 128,
645 doi:10.1007/JHEP06(2011)128, arXiv:1106.0522.
- 646 [36] H1 and ZEUS Collaboration, “HERAPDF1.5”, *Proceedings of the 35th International*
647 *Conference of High Energy Physics, Proceedings of Science* **168** (2010).

- 648 [37] G. A. Ladinsky and C. P. Yuan, “The nonperturbative regime in QCD resummation for
649 gauge boson production at hadron colliders”, *Phys. Rev.* **D50** (1994) 4239,
650 doi:10.1103/PhysRevD.50.R4239, arXiv:hep-ph/9311341.
- 651 [38] C. Balazs and C. P. Yuan, “Soft gluon effects on lepton pairs at hadron colliders”, *Phys.*
652 *Rev.* **D56** (1997) 5558–5583, doi:10.1103/PhysRevD.56.5558,
653 arXiv:hep-ph/9704258.
- 654 [39] F. Landry, R. Brock, P. M. Nadolsky, and C. P. Yuan, “Tevatron Run-1 Z boson data and
655 Collins-Soper-Sterman resummation formalism”, *Phys. Rev.* **D67** (2003) 073016,
656 doi:10.1103/PhysRevD.67.073016, arXiv:hep-ph/0212159.

DRAFT